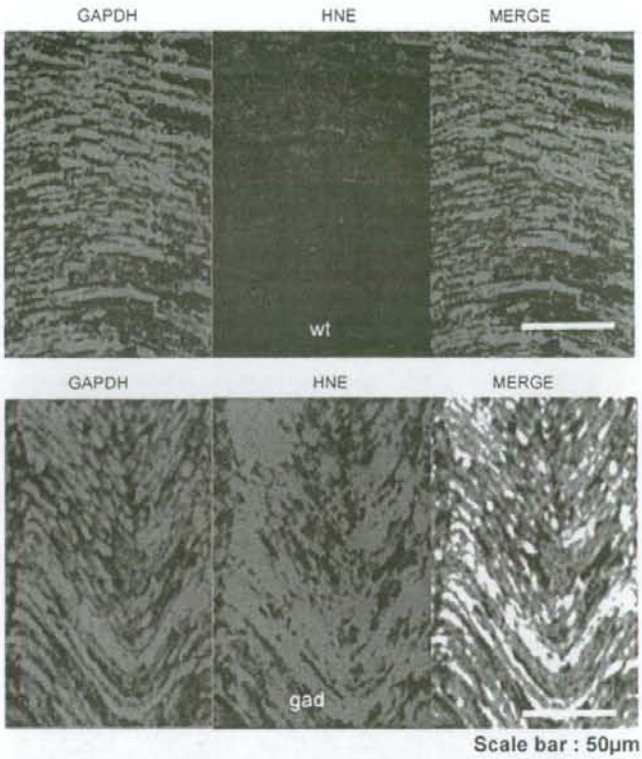

Fig. 6. Expression of HNE, a marker of oxidative stress, in the sciatic nerves of *gad* and WT mice.
Double immunofluorescent staining of sciatic nerves of *gad* and WT mice using antibodies against GAPDH and HNE. In WT mice, HNE was not detected (upper panel). On the other hand, HNE was strongly detected and mainly colocalized with GAPDH in *gad* mice (lower panel).

(Hara et al., 2006a). GAPDH has been reported to play roles in membrane fusion, microtubule bundling, nuclear RNA transport (Sirover, 1999), and transcription (Zheng et al., 2003). Particularly, its role as a mediator for cellular dysfunction/death has been highlighted (Sawa et al., 1997; Ishitani et al., 1998; Hara et al., 2005, 2006b). Sulfonation of GAPDH is reported to be induced by oxidative stress, and sulfonated GAPDH leads to cellular dysfunction (Hara et al., 2005, 2006a; Sen et al., 2008). Additionally, oxidative stress induces the oligomerization and aggregation of GAPDH through aberrant disulfide bonding of active-site cysteines, which leads to the formation of insoluble aggregates *in vitro* (Cumming and Schubert, 2005; Nakajima et al., 2007). Thus, GAPDH appears to participate in the mechanism leading to cellular dysfunction/death induced by oxidative stress. However, its function in axons or its association with axonal degeneration has not yet been demonstrated.

In this study, we found that GAPDH and sulfonated GAPDH were accumulated in *gad* mice compared with WT mice, suggesting that oxidative stress is increased in *gad* mice. In fact, we found that the oxidative stress marker HNE is increased in *gad* mice. It has also been reported that, the levels of carbonyl modification of proteins that is caused by oxidative stress are increased in the brains of *gad* mice compared with WT mice (Castegna et al., 2004). Therefore, we assume that accumulation of GAPDH and sulfonated GAPDH in the axons of *gad* mice were induced by oxidative stress.

Various molecules are involved in reduction-oxidative reactions, and recently the necessity of the UPS in reduction-oxidative reactions has been highlighted (Okada et al., 1999; Kang et al., 2008). It has been reported that a number of oxidative stress sensors are regulated by the UPS (Iwai, 2003; Kobayashi et al., 2004; Hara et al., 2006a). In *gad* mice, free-Ub pools are decreased in neurons, and proteolysis in the UPS is thought to be abnormal (Osaka et al., 2003). Oxidative stress is therefore expected to be increased in *gad* mice, which is consistent with our findings.

There is another possible mechanism for the accumulation of GAPDH in the axons of *gad* mice. GAPDH is reported to be degraded mainly by chaperone-mediated autophagy (Aniento et al., 1993; Cuervo et al., 1997). Our recent study showed that UCH-L1 physically interacts with lysosome-associated membrane protein type 2A, which is a component of CMA (Kabuta et al., 2008); thus CMA is possibly altered in the neuronal system of *gad* mice, potentially leading to the accumulation of GAPDH in the axons of *gad* mice.

This study demonstrates the alteration of GAPDH in axons of the *gad* mouse, a mutant with a loss of function of UCH-L1. Our findings suggest that GAPDH may participate in the process leading to the dying-back-type of axonal degeneration in *gad* mice and may provide valuable insight into the mechanisms of axonal degeneration.

Please cite this article in press as: Goto, A., et al., Proteomic and histochemical analysis of proteins involved in the dying-back-type of axonal degeneration in the gracile axonal dystrophy (*gad*) mouse. Neurochem. Int. (2009), doi:10.1016/j.neuint.2008.12.012

Acknowledgements

We thank the following people for their contributions to this work: Dr. Hidemitsu Nakajima (Osaka Prefecture University), Dr. Satoshi Nagamine (National Center of Neurology and Psychiatry) and Dr. Makoto R. Hara (Johns Hopkins University School of Medicine) for helpful discussions; Ms. Hisae Kikuchi (National Center of Neurology and Psychiatry) for technical assistance with tissue sections; Ms. Masako Shikama (National Center of Neurology and Psychiatry) for the care and breeding of animals; Dr. Hayato Onishi (University of Tokyo) for assistance with the TOF MASS analysis; and Dr. H. Akiko Popiel (National Center of Neurology and Psychiatry) for support with English; Mitsubishi Tanabe Pharma Corporation for giving a chance to A.G. of admission to doctoral course. This work was supported in part by Grants-in-Aid for Scientific Research from the Ministry of Health, Labour and Welfare of Japan, Grants-in-Aid for Scientific Research from the Ministry of Education, Culture, Sports, Science and Technology of Japan, the Program for Promotion of Fundamental Studies in Health Sciences of the National Institute of Biomedical Innovation, and a grant from Japan Science and Technology Agency.

References

Aniento, F., Roche, E., Cuervo, A.M., Knecht, E., 1993. Uptake and degradation of glyceraldehyde-3-phosphate dehydrogenase by rat liver lysosomes. J. Biol. Chem. 268, 10463–10470.

Castegna, A., Thongboonkerd, V., Klein, J., Lynn, B.C., Wang, Y.L., Osaka, H., Wada, K., Butterfield, D.A., 2004. Proteomic analysis of brain proteins in the gracile axonal dystrophy (gad) mouse, a syndrome that emanates from dysfunctional ubiquitin carboxyl-terminal hydrolase L-1, reveals oxidation of key proteins. J. Neurochem. 88, 1540–1546.

Chuang, D.M., Hough, C., Senatorov, V.V., 2005. Glyceraldehyde-3-phosphate dehydrogenase, apoptosis, and neurodegenerative diseases. Annu. Rev. Pharmacol. Toxicol. 45, 269–290.

Cuervo, A.M., Dice, J.F., Knecht, E., 1997. A population of rat liver lysosomes responsible for the selective uptake and degradation of cytosolic proteins. J. Biol. Chem. 272, 5606–5615.

Cumming, R.C., Schubert, D., 2005. Amyloid-beta induces disulfide bonding and aggregation of GAPDH in Alzheimer's disease. FASEB J. 19, 2060–2062.

Ferri, A., Sanes, J.R., Coleman, M.P., Cunningham, J.M., Kato, A.C., 2003. Inhibiting axon degeneration and synapse loss attenuates apoptosis and disease progression in a mouse model of motoneuron disease. Curr. Biol. 13, 669–673.

Fischer, L.R., Culver, D.G., Tennant, P., Davis, A.A., Wang, M., Castellano-Sanchez, A., Khan, J., Polak, M.A., Glass, J.D., 2004. Amyotrophic lateral sclerosis is a distal axonopathy: evidence in mice and man. Exp. Neurol. 185, 232–240.

Fischer, L.R., Glass, J.D., 2007. Axonal degeneration in motor neuron disease. Neurodegener. Dis. 4, 431–442.

Hara, M.R., Agrawal, N., Kim, S.F., Cascio, M.B., Fujimuro, M., Ozeki, Y., Takahashi, M., Cheah, J.H., Tankou, S.K., Hester, L.D., Ferris, C.D., Hayward, S.D., Snyder, S.H., Sawa, A., 2005. S-nitrosylated GAPDH initiates apoptotic cell death by nuclear translocation following Siah1 binding. Nat. Cell. Biol. 7, 665–674.

Hara, M.R., Cascio, M.B., Sawa, A., 2006a. GAPDH as a sensor of NO stress. Biochim. Biophys. Acta 1762, 502–509.

Hara, M.R., Thomas, B., Cascio, M.B., Bae, B.I., Hester, L.D., Dawson, V.L., Dawson, T.M., Sawa, A., Snyder, S.H., 2006b. Neuroprotection by pharmacologic blockade of the GAPDH death cascade. Proc. Natl. Acad. Sci. U.S.A. 103, 3887–3889.

Harada, T., Harada, C., Wang, Y.L., Osaka, H., Amanai, K., Tanaka, K., Takizawa, S., Setsuie, R., Sakurai, M., Sato, Y., Noda, M., Wada, K., 2004. Role of ubiquitin carboxy terminal hydrolase-L1 in neural cell apoptosis induced by ischemic retinal injury in vivo. Am. J. Pathol. 164, 59–64.

Ishitani, R., Tanaka, M., Sunaga, K., Katsube, N., Chuang, D.M., 1998. Nuclear localization of overexpressed glyceraldehyde-3-phosphate dehydrogenase in cultured cerebellar neurons undergoing apoptosis. Mol. Pharmacol. 53, 701–707.

Iwai, K., 2003. An ubiquitin ligase recognizing a protein oxidized by iron: implications for the turnover of oxidatively damaged proteins. J. Biochem. 134, 175–182.

Kabuta, T., Furuta, A., Aoki, S., Furuta, K., Wada, K., 2008. Aberrant interaction between Parkinson disease-associated mutant UCH-L1 and the lysosomal receptor for chaperone-mediated autophagy. J. Biol. Chem. 283, 23731–23738.

Kang, S.I., Choi, H.W., Kim, I.Y., 2008. Redox-mediated modification of PLZF by SUMO-1 and ubiquitin. Biochem. Biophys. Res. Commun. 369, 1209–1214.

Kikuchi, T., Mukoyama, M., Yamazaki, K., Moriya, H., 1990. Axonal degeneration of ascending sensory neurons in gracile axonal dystrophy mutant mouse. Acta Neuropathol. 80, 145–151.

Knowles, M.R., Cervino, S., Skynner, H.A., Hunt, S.P., de Felipe, C., Salim, K., Meneses-Lorente, G., McAllister, G., Guest, P.C., 2003. Multiplex proteomic analysis by two-dimensional differential in-gel electrophoresis. Proteomics 3, 1162–1171.

Kobayashi, A., Kang, M.I., Okawa, H., Ohtsuji, M., Zenke, Y., Chiba, T., Igarashi, K., Yamamoto, M., 2004. Oxidative stress sensor Keap1 functions as an adaptor for Cul3-based E3 ligase to regulate proteasomal degradation of Nrf2. Mol. Cell. Biol. 24, 7130–7139.

Larsen, C.N., Krantz, B.A., Wilkinson, K.D., 1998. Substrate specificity of deubiquitinating enzymes: ubiquitin C-terminal hydrolases. Biochemistry 37, 3358–3368.

Li, H., Li, S.H., Yu, Z.X., Shelbourne, P., Li, X.J., 2001. Huntingtin aggregate-associated axonal degeneration is an early pathological event in Huntington's disease mice. J. Neurosci. 21, 8473–8481.

Liu, Y., Fallon, L., Lashuel, H.A., Liu, Z., Lansbury Jr., P.T., 2002. The UCH-L1 gene encodes two opposing enzymatic activities that affect alpha-synuclein degradation and Parkinson's disease susceptibility. Cell 111, 209–218.

Miura, H., Oda, K., Endo, C., Yamazaki, K., Shibasaki, H., Kikuchi, T., 1993. Progressive degeneration of motor nerve terminals in GAD mutant mouse with hereditary sensory axonopathy. Neuropathol. Appl. Neurobiol. 19, 41–51.

Mukoyama, M., Yamazaki, K., Kikuchi, T., Tomita, T., 1989. Neuropathology of gracile axonal dystrophy (GAD) mouse. An animal model of central distal axonopathy in primary sensory neurons. Acta Neuropathol. 79, 294–299.

Nakajima, H., Amano, W., Fujita, A., Fukuhara, A., Azuma, Y.T., Hata, F., Inui, T., Takeuchi, T., 2007. The active site cysteine of the proapoptotic protein glyceraldehyde-3-phosphate dehydrogenase is essential in oxidative stress-induced aggregation and cell death. J. Biol. Chem. 282, 26562–26574.

Oda, K., Yamazaki, K., Miura, H., Shibasaki, H., Kikuchi, T., 1992. Dying back type axonal degeneration of sensory nerve terminals in muscle spindles of the gracile axonal dystrophy (GAD) mutant mouse. Neuropathol. Appl. Neurobiol. 18, 265–281.

Okada, K., Wangpoengtrakul, C., Osawa, T., Toyokuni, S., Tanaka, K., Uchida, K., 1999. 4-Hydroxy-2-nonenal-mediated impairment of intracellular proteolysis during oxidative stress. Identification of proteasomes as target molecules. J. Biol. Chem. 274, 23787–23793.

Osaka, H., Wang, Y.L., Takada, K., Takizawa, S., Setsuie, R., Li, H., Sato, Y., Nishikawa, K., Sun, Y.J., Sakurai, M., Harada, T., Hara, Y., Kimura, I., Chiba, S., Namikawa, K., Kiyama, H., Noda, M., Aoki, S., Wada, K., 2003. Ubiquitin carboxy-terminal hydrolase L1 binds to and stabilizes monoubiquitin in neuron. Hum. Mol. Genet. 12, 1945–1958.

Saigoh, K., Wang, Y.L., Suh, J.G., Yamanishi, T., Sakai, Y., Kiyosawa, H., Harada, T., Ichihara, N., Wakana, S., Kikuchi, T., Wada, K., 1999. Intragenic deletion in the gene encoding ubiquitin carboxy-terminal hydrolase in gad mice. Nat. Genet. 23, 47–51.

Sawa, A., Khan, A.A., Hester, L.D., Snyder, S.H., 1997. Glyceraldehyde-3-phosphate dehydrogenase: nuclear translocation participates in neuronal and nonneuronal cell death. Proc. Natl. Acad. Sci. U.S.A. 94, 11669–11674.

Sen, N., Hara, M.R., Kornberg, M.D., Cascio, M.B., Bae, B.I., Shahani, N., Thomas, B., Dawson, T.M., Dawson, V.L., Snyder, S.H., Sawa, A., 2008. Nitric oxide-induced nuclear GAPDH activates p300/CBP and mediates apoptosis. Nat. Cell. Biol. 10, 866–873.

Shaw, M.M., Riederer, B.M., 2003. Sample preparation for two-dimensional gel electrophoresis. Proteomics 3, 1408–1417.

Sirover, M.A., 1999. New insights into an old protein: the functional diversity of mammalian glyceraldehyde-3-phosphate dehydrogenase. Biochim. Biophys. Acta 1432, 159–184.

Stokin, G.B., Lillo, C., Falzone, T.L., Brusch, R.G., Rockenstein, E., Mount, S.L., Raman, R., Davies, P., Masliah, E., Williams, D.S., Goldstein, L.S., 2005. Axonopathy and transport deficits early in the pathogenesis of Alzheimer's disease. Science 307, 1282–1288.

Wang, Y.L., Takeda, A., Osaka, H., Hara, Y., Furuta, A., Setsuie, R., Sun, Y.J., Kwon, J., Sato, Y., Sakurai, M., Noda, M., Yoshikawa, Y., Wada, K., 2004. Accumulation of beta- and gamma-synucleins in the ubiquitin carboxyl-terminal hydrolase L1-deficient gad mouse. Brain Res. 1019, 1–9.

Wilkinson, K.D., Lee, K.M., Deshpande, S., Duerksen-Hughes, P., Boss, J.M., Pohl, J., 1989. The neuron-specific protein PGP 9.5 is a ubiquitin carboxyl-terminal hydrolase. Science 246, 670–673.

Yamazaki, K., Wakasugi, N., Tomita, T., Kikuchi, T., Mukoyama, M., Ando, K., 1988. Gracile axonal dystrophy (GAD), a new neurological mutant in the mouse. Proc. Soc. Exp. Biol. Med. 187, 209–215.

Zheng, L., Roeder, R.G., Luo, Y., 2003. S phase activation of the histone H2B promoter by OCA-S, a coactivator complex that contains GAPDH as a key component. Cell 114, 255–266.

Please cite this article in press as: Goto, A., et al., Proteomic and histochemical analysis of proteins involved in the dying-back-type of axonal degeneration in the gracile axonal dystrophy (*gad*) mouse. Neurochem. Int. (2009), doi:10.1016/j.neuint.2008.12.012

Neurochemistry International xxx (2009) xxx–xxx

Contents lists available at ScienceDirect

Neurochemistry International

journal homepage: www.elsevier.com/locate/neuint

Ubiquitin dimers control the hydrolase activity of UCH-L3

Rieko Setsuie [a], Mikako Sakurai [a,1], Yuriko Sakaguchi [b], Keiji Wada [a,*]

[a] Department of Degenerative Neurological Diseases, National Institute of Neuroscience, National Center of Neurology and Psychiatry, 4-1-1 Ogawahigashi, Kodaira, Tokyo 187-8502, Japan
[b] Department of Chemistry and Biotechnology, Graduate School of Engineering, The University of Tokyo, Bunkyo-ku, Tokyo, Japan

ARTICLE INFO

Article history:
Received 29 September 2008
Received in revised form 3 December 2008
Accepted 15 December 2008

Keywords:
Ubiquitin
Ubiquitin dimer
Ubiquitin carboxy terminal hydrolase-L1 (UCH-L1)
Ubiquitin carboxy terminal hydrolase-L3 (UCH-L3)

ABSTRACT

Ubiquitin (Ub) carboxy terminal hydrolase (UCH)-L1 and UCH-L3 are two of the deubiquitinating enzymes expressed in the brain. Both *gad* mice, which lack UCH-L1 expression and *Uchl3* knockout mice exhibit neurodegeneration, although at distinct areas. These phenotypes indicate the importance of UCH-L1 and UCH-L3 in the regulation of the central nervous system. However, molecular substrates and the molecular regulators of UCH-L1 and UCH-L3 remain poorly identified. Here we show that Ub dimers interact non-covalently with UCH-L3 *in vitro* and in cells. These interactions were not observed with UCH-L1 in cells. *In vitro*, K48-linked Ub dimers pronouncedly inhibited the hydrolase activity of UCH-L3, while mono-Ub, a previously identified interacting protein, inhibited the hydrolase activity of UCH-L1. These results indicate that mono-Ub and Ub dimers may regulate the enzymatic functions of UCH-L1 and UCH-L3, respectively, *in vivo*.

1. Introduction

The ubiquitin (Ub) system is involved in the regulation of various physiological phenomena including development, inflammatory response, and intracellular trafficking (Hershko and Ciechanover, 1998; Hicke, 2001; Glickman and Ciechanover, 2002; Mukhopadhyay and Riezman, 2007). Malfunction of the Ub system in the central nervous system (CNS) may lead to neurodegeneration or synaptic dysfunction (Rubinsztein, 2006; Hegde and Upadhya, 2007). Ub can be covalently conjugated to substrate proteins by the sequential action of E1, E2 and E3 enzymes forming an isopeptide bond between the carboxy terminus of Ub and the lysine residues of the substrates (Hershko and Ciechanover, 1998). The attachment of Ub to the substrates may occur either in the form of a single Ub or a poly-Ub chain, where the carboxy terminus of one Ub moiety is covalently linked to one of the seven Lys residues of an adjacent Ub molecule.

Deubiquitination involves the hydrolysis of the isopeptide bonds between the carboxy terminus glycine of the Ub and the lysine of the substrates or Ub, which requires the activity of deubiquitinating enzymes (DUBs) (Nijman et al., 2005). DUBs can be divided into six distinct families: the Ub-specific processing proteases, the Ub carboxyl-terminal hydrolases (UCHs), the Ataxin-3/Josephin domains, the ovarian tumor domain-containing proteases, the viral processing proteases and the JAMM proteases.

UCH is a cysteine protease with relatively small molecular weight. There is one UCH in yeast, and four UCH isozymes in mammals: UCH-L1, UCH-L3, UCH37 and BAP1. Of these, UCH-L1 and UCH-L3 are the most closely related family members with about 53% identity. These UCHs have also been shown to hydrolyze Nedd8 (neural precursor cell expressed developmentally down regulated 8), a Ub-like protein with 68% identity to Ub (Wada et al., 1998; Hemelaar et al., 2004). The expression of UCH-L3 is ubiquitous whereas that of UCH-L1 is mainly restricted to the brain and the testis/ovary (Wilkinson et al., 1989; Kurihara et al., 2000; Kurihara et al., 2001).

Previous studies using mutant mice of *Uchl1* and *Uchl3* indicated that these enzymes are involved in the regulation of the brain function (Setsuie and Wada, 2007). The I93M point mutation in UCH-L1 is associated with familial Parkinson's disease (Leroy et al., 1998) and we have previously shown that I93M UCH-L1 expression in the cell or in transgenic mice induces dopaminergic neuron death (Setsuie et al., 2007; Kabuta et al., 2008). We also reported that *gad* (gracile axonal dystrophy) mice, which lack Uchl1 expression, show axonal degeneration of the gracile tract, which results in sensory ataxia (Saigoh et al., 1999). Our analysis also indicated that UCH-L1 is involved in many biological aspects including neuronal apoptosis (Harada et al., 2004), neurotransmitter receptor activation (Manago et al., 2005), neural progenitor regulation (Sakurai et al., 2006), learning and memory (Sakurai et al., 2008). On the other hand, UCH-L3 knockout mice show photoreceptor cell degeneration (Semenova

* Corresponding author. Tel.: +81 42 346 1715; fax: +81 42 346 1745.
E-mail address: wada@ncnp.go.jp (K. Wada).
[1] Present address: Department of Pathology and Taub Institute, Columbia University, New York, NY 10032, USA.

0197-0186/$ – see front matter © 2008 Elsevier Ltd. All rights reserved.
doi:10.1016/j.neuint.2008.12.013

Please cite this article in press as: Setsuie, R., et al., Ubiquitin dimers control the hydrolase activity of UCH-L3. Neurochem. Int. (2009), doi:10.1016/j.neuint.2008.12.013

et al., 2003; Sano et al., 2006) and defects in memory function (Wood et al., 2005). These different phenotypes of mutant mice indicate that although both enzymes share similar properties in terms of biochemical identity (Johnston et al., 1997; Larsen et al., 1998; Misaghi et al., 2005; Das et al., 2006), UCH-L1 and UCH-L3 should be differentially controlled or be regulated by distinct molecules.

To identify the proteins that regulate UCH-L1 and UCH-L3 in a diverse manner, we performed immunoaffinity purification assay using UCH-L1 and UCH-L3 and found that UCH-L3 is inhibited by Ub dimers (di-Ub) while UCH-L1 is inhibited by mono-Ub.

2. Experimental procedures

2.1. Isolation and culture of mouse embryonic fibroblasts (MEFs) and their immortalization

Pregnant female *Uchl3* heterozygote mice (Kurihara et al., 2000) were sacrificed at 14–15 days postcoitus. The head, the viscera and the bones of each embryo were removed under a dissecting microscope and a part of these samples were used for genotyping. The remaining portion of embryo was placed in 0.25% trypsin-EDTA (Invitrogen, Carlsbad, CA, USA), cut finely with razor blade, and incubated for 15 min at 37 °C. The cell suspension was passed several times through a 1 ml pipette tip until no clumps were visible. The cell suspension prepared from each individual embryo was washed with medium containing 10% (v/v) fetal bovine serum (FBS). Viable cells were determined by trypan-blue exclusion assay and 4,000,000 viable cells from each embryo were plated in 100 mm culture dishes. MEFs were maintained in Dulbecco's Modified Eagle's Medium (Sigma, St. Louis, MO, USA) supplemented with 10% (v/v) FBS (JRH, Biosciences, Lenexa, KS, USA), 100 U/ml penicillin and streptomycin (Invitrogen). The genotype was determined using the remnants of tissues, and polymerase chain reactions (PCR) were conducted using the primers and the thermal cycling as follows: L3KO-1 primer (5′-ggaactactgagccatatgtgc-3′) L3KO-2 primer (5′-cggacttactccatcacttcac-3′) L3KO-3 primer (5′-cttgtgagcgccaagtgc-3′), one cycle of 98 °C for 5 min, 30 cycles at 98 °C for 10 s, 60 °C for 20 s, and 72 °C for 30 s. For the immortalization of MEFs, basic 3T3 protocols were carried out as described (Todaro and Green, 1963).

2.2. Construction of cell lines expressing human wild-type or mutant UCH-L3

Retrovirus vectors encoding human wild-type UCH-L3 were constructed as follows. Full-length human UCH-L3 cDNA was cloned from human liver cDNA library and inserted into the pGEM-T vector (Promega, Madison, WI, USA). For PCR-based amplification of the insert, the huchl3-retro-s2 primer (5′-GGGGCTCGAGCGCCG-CATGGAGGGTCAACGCTGGCT-3′) and huchl3-pci-as1 primer (5′-GGGGGCGGCC-GCCTATGCTGCAGAAAGAGC AATCG-3′) were used with 35 cycles of 94 °C for 30 s, 55 °C for 30 s and 72 °C for 1 min. The amplified PCR fragment and pOZ-N retrovirus vector were successively digested with XhoI and NotI. The enzymatically digested PCR fragment and pOZ-N vector were subsequently applied to electrophoresis, gel extraction and ligated using the ligation system ver2 (Takara, Tokyo, Japan). This resulted in the insertion of human UCH-L3 without a starting methionine after the HA and FLAG double-tag sequence between the XhoI and NotI sites at the multicloning site of the pOZ-N double-tag retrovirus vector. To obtain Ub hydrolase-deficient C95S mutant- and Ub affinity deficient D33A mutant-encoding retrovirus vectors, the Cys95 or Asp33 of hUCH-L3 were mutated to Ser or Ala, respectively, using PCR-based *in vitro* mutagenesis (Stratagene, La Jolla, CA, USA). The primers used for mutagenesis were huchl3-C95S-s1 (5′-ATCAGCAATGCAATGCCTGTGGAAC AATTGGA-3′), hchl3-C95S-as1 (5′-TCCAATTGTTCCACAGGCATTGCTGAT-3′), huchl3-D33A-s (5′-CTAACT-GGCAATTCGTTGCTGTATATGGAATGGATCC TGAAC-3′) and huchl3-D33A-as (5′-GTTCAGGATCCATTCCATATA CAGCAACGAATTGCCAGTTAG-3′). The human UHCL1 or GFP cDNA derived inserts were cloned into the XhoI and NotI site of the same retrovirus vector, as described previously (Sakurai et al., 2006). The production of retroviruses and cell lines were conducted as described elsewhere (Ogawa et al., 2002).

2.3. Immunoprecipitation

2.5×10^8 floating Hela cells expressing FLAG-HA tagged hUCH-L3 were collected and washed with phosphate buffered saline (PBS) twice and the cell pellets were stored at −80 °C until all of the clones were ready for lysis. The floating Hela cells were quickly thawed at 37 °C, suspended in 15 ml of ice-cold modified RIPA buffer (50 mM Tris–HCl (pH 7.4), 1% Nonidet P40, 0.25% sodium deoxycholate, 150 mM NaCl, 1 mM EDTA, 1 mM $NaVO_4$, 1 mM NaF with Complete EDTA-free protease inhibitors (Roche Diagnostics, Indianapolis, IN, USA)), and kept on ice for 30 min. After three repeated sonications for 10 s with 30 s intervals, lysates were centrifuged at 12,000 rpm at 4 °C for 10 min using a swing-rotor type centrifuge. The supernatant was recovered for further purification and aliquots were kept at −80 °C as a pre-immunoprecipitation lysate. To the remaining supernatant, anti-FLAG M2 antibody-conjugated agarose (Sigma) in 600 μl slurry was added and gently rotated at 4 °C for 8 h. After rotation, the samples were poured into the empty column (Bio-Rad, Hercules, CA, USA), washed four times with 8 ml 0.1 B buffer (20 mM Tris–HCl (pH 8.0), 0.1 M KCl, 5 mM $MgCl_2$, 10% glycerol, 0.1% Tween-20, 10 mM β-mercaptoethanol, 0.2 mM PMSF), and briefly centrifuged to remove the excess washing buffer. After capping the bottom of the column, 600 μl elution buffer (160 μg/ml of 3× FLAG peptide in 0.1 B buffer) were added to the column, rotated at 4 °C for 1 h, and eluted into an eppendorf tube. This elution step was repeated and a total of 1.2 ml eluate was used for the second purification. The second purification was performed using the anti-HA antibody (clone 12CA5)-conjugated agarose. The steps were the same as for FLAG purification except that the scale was minimized with 100 μl of elution (1 mg/ml HA peptide (Roche) in 0.1 B buffer). The resulting final eluates were kept at −80 °C until analysis.

2.4. Mass spectrometry analysis

After the negative staining (Nakalai Tesque Inc., Kyoto, Japan) of the SDS-PAGE gels, protein bands were sliced from the gel, reduced, S-alkylated, and subjected to in-gel trypsin digestion. The digested peptides were extracted with 50% acetonitrile and 0.1% trifluoroacetic acid and subjected to liquid-chromatography tandem mass spectrometry (LC–MS/MS) analysis.

2.5. Silver staining and Western blotting

Silver staining was done using the Daiichi Silver staining Kit (Daiichi, Tokyo, Japan). For the Western blotting of UCH-L3 or HA-FLAG tagged UCH-L3, 15% mini gels (DRC, Tokyo, Japan) were used. For the detection of mono- or di-Ub, or Nedd8, 15–20% gradient mini gels (DRC) were used. For 2D-Western blotting, samples were loaded on 4–11 N IPG strips (GE Healthcare UK Ltd., Buckinghamshire, England) using IPGphor and the second dimension was run on 15–20% gradient gels (DRC). The antibodies used were anti-HA antibody (clone 12CA5, 1:1,000), anti-FLAG M2 antibody (Sigma; 1:1000), anti-Ub antibody (Sigma; 1:1000 or Dako; 1:1000), anti-Nedd8 antibody (Cell signaling; 1:1000) anti-UCH-L1 antibody (Ultraclone RA95101; 1:5000, England, UK) and anti-UCH-L3 antibody ((Kwon et al., 2004); 1:1,000). HRP-conjugated secondary antibodies were from Pierce and signals were detected using a chemiluminescent Super Signal West Dura Extended Duration Substrate kit or West Femto Maximum Sensitivity Substrate kit (Pierce, Rochford, IL) and analyzed with a ChemiImager (Alpha Innotech, San Leandro, CA). The protein marker was purchased from Bio-Rad.

2.6. Pull-down assay

6HN-tagged human UCH-L3 and UCH-L1 proteins were prepared as described previously (Nishikawa et al., 2003). Pull-down assay was conducted as described previously with some modifications (Kabuta et al., 2008). In brief, 6 μg 6HN-UCH and 4 μg of either K48-linked di-Ub, K63-linked di-Ub, or linear di-Ub (all from Boston Biochem, Cambrige, MA, USA), were mixed in the presence of 0.1 μg/ml BSA in tris-buffered saline (TBS) at 4 °C for 2 h. Fifty micro liters of TALON resin (Clontech, Palo Alto, CA, USA) were added to samples and incubated at 4 °C for 1 h. After washing the resin five times with PBS in the presence of 20 mM imidazole and 0.05% Tween-20, the bound proteins were eluted with SDS sample buffer.

2.7. Ubiquitin hydrolase activity assay

The Ub hydrolase activity assay, using recombinant UCH-L3 and Ub-AMC (both from Boston Biochem), was performed as described previously (Nishikawa et al., 2003), in the presence or absence of di-Ub.

3. Results

3.1. UCH-L3 but not UCH-L1 interacts with di-Ub

To identify the proteins that interact with UCH-L1 or UCH-L3, which might represent the potential substrates or the functional effecters, we performed immunoaffinity chromatography. Floating Hela cells that stably expressed human UCH-L3 tagged with the FLAG-HA epitope at its N-terminus (L3 WT), UCH-L3 C95S (active site mutant of UCH-L3), UCH-L1 (L1 WT), UCH-L1 C90S (active site mutant of UCH-L1), GFP and Mock were constructed (Fig. 1A). Western blotting using anti-HA and anti-FLAG antibodies detected a single band at the appropriate molecular weight in each cell line indicating FLAG-HA tagged proteins were sufficiently expressed and at comparable levels (Fig. 1A). We detected two bands with the anti-UCH-L3 antibody in all of the cell lines; these bands correspond to the exogenously expressed and endogenously expressed UCH-L3 in Hela cells (Fig. 1A).

Please cite this article in press as: Setsuie, R., et al., Ubiquitin dimers control the hydrolase activity of UCH-L3. Neurochem. Int. (2009), doi:10.1016/j.neuint.2008.12.013

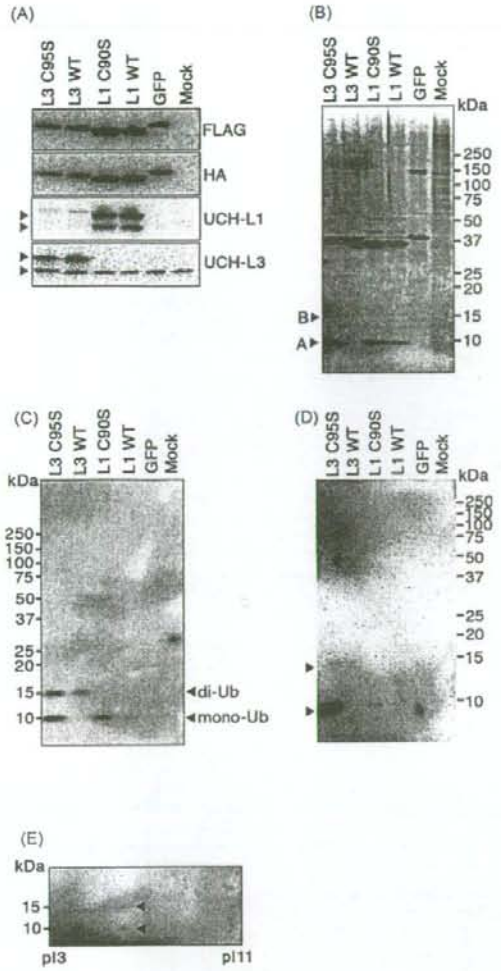

Fig. 1. Di-Ub interacts with UCH-L3. (A) Floating Hela cells stably expressing FLAG-HA double-tagged UCH-L3 or UCH-L1 were constructed. The expression of exogenous UCH-L3 or UCH-L1 was confirmed by anti-FLAG, anti-HA, anti-UCH-L1 and anti-UCH-L3 antibodies. Anti-UCH-L1 antibody showed two bands (indicated by the arrows), where upper band corresponds to the predicted molecular weight of UCH-L1 including FLAG-HA tag at the N-terminal. The lower band may indicate the N-terminally processed form of UCH-L1, which lack FLAG-HA tag. Anti-UCH-L3 antibody also showed two bands, where lower band represent the endogenous UCH-L3 expressed in Hela cells. (B) Silver staining of proteins, which are obtained by the sequential immunoaffinity purification using anti-FLAG antibody-conjugated agarose and anti-HA antibody-conjugated agarose. The bands, which are indicated by the arrow A and B were excised and processed for LC–MS/MS analysis. (C) Western blotting of the proteins as in (B) with anti-Ub antibody from Sigma–Aldrich. Note the presence of anti-Ub antibody immunoreactive bands at about 10 kDa and 15 kDa, which represent mono- and di-Ub. (D) Western blotting of the proteins as in (B) with anti-Nedd8 antibody from Cell Signaling. Note the presence of anti-Nedd8 antibody immunoreactive bands at about 10 kDa and 15 kDa, which may represent mono- and di-Nedd8. (E) 2D-Western blotting of the proteins, which is obtained by the sequential immunoaffinity purification of UCH-L3 C95S expressing Hela cell lysate as in (B). Anti-Ub antibody from Sigma–Aldrich is used.

UCH-L1- or UCH-L3-containing complexes were affinity purified from stable cells using anti-FLAG antibody-conjugated agarose, followed by anti-HA antibody-conjugated agarose and each elution was conducted under native conditions using 3×

Table 1
The amino acid sequences of fragments detected by the mass spectrometric analysis of bands A and B from Fig. 1B.

Band	Amino acid sequences
A	MQIFVKTLTG KTITLEVEPS DTIENVKAKI QDKEGIPPDQ QRLIFAGKQL EDGRTLSDYN IQKESTLHLV LRLRGG
B	MQIFVKTLTG KTITLEVEPS DTIENVKAKI QDKEGIPPDQ QRLIFAGKQL EDGRTLSDYN IQKESTLHLV LRLRGG

The bands, from the immunoaffinity-purified complex of C95S mutant corresponding to A and B of Fig. 1B, are excised and subjected to LC–MS/MS analysis as described in the Section 2, and the amino acid sequences in red are detected fragments by LC–MS/MS analysis.

FLAG peptide or HA peptide. After the second immunoaffinity chromatography, proteins associated with UCH-L3 WT, UCH-L3 C95S, UCH-L1 WT and UCH-L1 C90S were identified by SDS-PAGE followed by silver staining (Fig. 1B). The deduced amino acid sequences, which were obtained from the LC–MS/MS analysis, indicate that the bands with a molecular weight of about 9 kDa (arrow A) in Fig. 1B correspond to the free mono-Ub (Table 1). Consistently, the immunoblotting of immunoaffinity-purified proteins with anti-Ub antibody, which recognizes both free Ub and ubiquitylated proteins, revealed that these bands represent free mono-Ub (Fig. 1C). The finding that UCH-L1 and the UCH-L1 C90S mutant have strong affinity for mono-Ub is consistent with our previous finding that UCH-L1 interacts with and stabilizes free mono-Ub *in vivo* (Osaka et al., 2003). The strong detection of mono-Ub with the UCH-L3 C95S mutant complex but not with the UCH-L3 WT complex indicates that C95S mutation leads to either the conformational change resulting in the strong interaction with mono-Ub, or the lack of hydrolase activity that results in the interaction with the substrate.

The molecule with molecular weight of about 15 kDa (arrow B in Fig. 1B) identified for the UCH-L3 WT and UCH-L3 C95S immunoaffinity-purified proteins, and which had Ub sequence within this molecule, was of interest because this molecule was specific to UCH-L3 and not UCH-L1. Although the molecular weight is greater than for free mono-Ub, LC–MS/MS analysis of this band only revealed Ub (Table 1). It is known that free di-Ub has a size of about 15 kDa. To confirm whether the bands at 15 kDa (arrow B in Fig. 1B) are, in fact, free di-Ub, we performed 2D-Western blotting of the C95S immunoaffinity-purified complex using the anti-Ub antibody. The *p*I of di-Ub should be similar to that of mono-Ub. As shown in Fig. 1E, the 15 kDa molecule (upper arrow in Fig. 1E) had a *p*I similar to that of free mono-Ub (lower arrow in Fig. 1E), indicating that the band may represent di-Ub.

To confirm the direct interaction of di-Ub and UCH-L3, we performed pull-down assays using recombinant mono-Ub or di-Ub and UCH-L3. As shown in Fig. 2B, UCH-L3 can form physiological complexes not only with di-Ub but also with mono-Ub. However, the affinity of UCH-L3 to mono-Ub is weak compared to di-Ub (see Fig. 1B, C and Fig. 2A).

Nedd8, an Ub-like protein with 57% identity to Ub, is a previously reported UCH-L3 and UCH-L1 interacting protein (Wada et al., 1998; Hemelaar et al., 2004). Although we did not detect any derivatives of Nedd8 on LC–MS/MS analysis, Western blotting analysis of immunoaffinity-purified complexes using the anti-Nedd8 antibody revealed several bands, which presumably represent mono-Nedd8 (lower arrow in Fig. 1D) and di-Nedd8 (upper arrow in Fig. 1D).

Please cite this article in press as: Setsuie, R., et al., Ubiquitin dimers control the hydrolase activity of UCH-L3. Neurochem. Int. (2009), doi:10.1016/j.neuint.2008.12.013

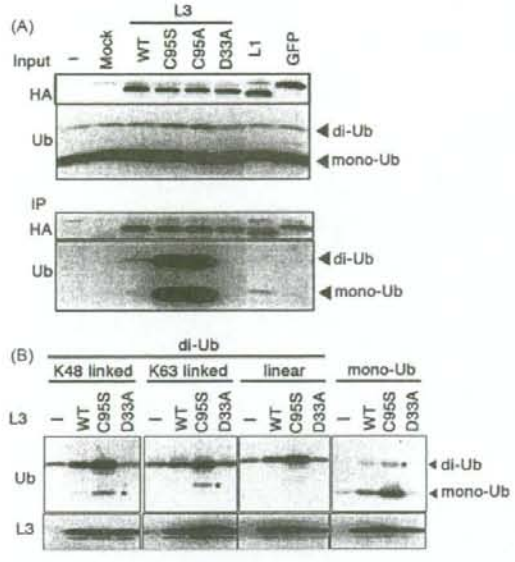

Fig. 2. C95 and D33 of UCH-L3 are involved in the interaction with K48-linked, or K63-linked or linear di-Ub. (A) UCH-L3 interacting proteins were co-immunoprecipitated from Hela cells expressing FLAG-HA tagged UCH-L3 mutants. Cell lysates were immunoprecipitated using anti-HA antibody and co-immunoprecepitates were analyzed by anti-Ub antibody from Sigma–Aldrich. Note the presence of di-Ub in UCH-L3 WT or C95S mutant or C95A mutant immunoprecipitates but not in UCH-L3 D33A mutant or UCH-L1 immunoprecipitates. (B) *In vitro* pull-down assays using recombinant UCH-L3 and recombinant di-Ub or mono-Ub. The pulled-down samples were analyzed by anti-UCH-L3 antibody and anti-Ub antibody from DAKO. UCH-L3 WT and C95S mutant interacted with K48-linked, or K63-linked or linear di-Ub or mono-Ub while these interactions were diminished with D33A mutant. The bands with the asterisks are unidentified molecules, which is presumably derived from the contaminants of di-Ub or mono-Ub.

3.2. Di-ubiquitin interacts directly with UCH-L3 via hydrolytic active site

NMR studies and X-ray studies of UCHs complexed with Ub derivatives indicated that D33 of UCH-L3 is important for its affinity to Ub (Wilkinson et al., 1999; Misaghi et al., 2005). To confirm whether this amino acid is also responsible for the interaction of di-Ub with UCH-L3, we performed an immunoprecipitation assay using mutant UCH-L3. FLAG-HA tagged UCH-L3 WT, C95S, C95A, D33A mutants and UCH-L1 expressing Hela cells were immunoprecipitated with anti-HA antibody-conjugated agarose. As shown in Fig. 2A, the D33A mutation diminished the interaction of di-Ub with UCH-L3 while the C95S and the C95A mutations enhanced the interaction.

The first methionine and seven internal lysine residues of Ub are known to form isopeptide bonds with the carboxy terminus glycine of an adjacent Ub molecule (Kirkpatrick et al., 2005; Kirisako et al., 2006). Thus, eight various forms of di-Ub may exist. However, only K48 and K63-linked di-Ub are presumed to exist with relative abundance *in vivo* with the former being identified *in vivo* (van Nocker and Vierstra, 1993; Hochstrasser, 2006). In addition, previous studies raised the possibility that tandemly conjugated di-Ub may form after processing of the Ub gene products by the DUBs (Wilkinson, 1997). Thus, we assessed whether these di-Ubs (linear, K48-linked and K63-linked) can interact with UCH-L3 *in vitro*. The pull-down analysis of di-Ub with 6HN-tagged UCH-L3 indicated that the K48-linked, K63-linked and linear di-Ub all interacted with UCH-L3 (Fig. 2B). In addition, the pull-down analysis of di-Ub using the D33A mutant abolished the interaction, while the C95S mutant increased the interaction. These results also indicate that D33 and C95 of UCH-L3 are amino acid residues that are involved in the interaction with di-Ub.

3.3. Exogenously expressed UCH-L3 does not hydrolyze di-Ub in cells

We have shown that UCH-L3 interacts with free di-Ub. The previous *in vitro* studies using recombinant human UCH-L3 showed that UCH-L3 neither have the activity toward hydrolyzing tandemly conjugated di-Ub or K48-linked di-Ub though it can hydrolyze Ub conjugates with small adducts less than 20 amino acids or nucleophils such as glutathione (Larsen et al., 1998). To confirm that di-Ubs are not the substrate of UCH-L3, we also performed hydrolase assays using K48-linked, K63-linked and linear di-Ub as the substrates *in vitro*. After incubation for 24 h, UCH-L3 did not produce mono-Ub from these three forms of di-Ub (data not shown), which is consistent with previous reports (Larsen et al., 1998). Although UCH-L3 did not show hydrolase activity toward the K48-linked, K63-linked or linear di-Ub, there exists the possibility that other forms of di-Ub (presumably K11-linked, K27-linked, K29-linked and K33-linked di-Ubs) may be hydrolyzed by UCH-L3. To eliminate this possibility, we analyzed stable cell lines expressing several functional mutants of UCH-L3 and determined whether di-Ub accumulates in the absence of UCH-L3 hydrolase activity.

Two immortalized 3T3 cell lines derived from two different UCH-L3 knockout mouse embryonic fibroblasts were generated and used to make stable cell lines either expressing WT UCH-L3, its mutants C95S, D33A, UCH-L1 or GFP. The same retrovirus systems were used as in Fig. 1, resulting in the attachment of FLAG-HA tags to each exogenous protein. Cell lysates were immunoblotted using anti-HA, anti-UCH-L1, and anti-UCH-L3 antibodies (Fig. 3A). The absence of endogenous UCH-L1 or UCH-L3 and the presence of exogenous proteins at comparable levels were assessed in these cells (Fig. 3A). The immunoprecipitation assays of several UCH-L3 mutants indicated that the D33A mutant lost the affinity to interact with di-Ub while the C95S mutant retained this function (Fig. 2A). In this condition, immunoblotting with the anti-Ub antibody was performed. We presumed that, if UCH-L3 functions to hydrolyze free di-Ub *in vivo*, the free di-Ub would accumulate in cells not expressing the WT UCH-L3. However, cells expressing WT UCH-L3 showed increasing levels of free di-Ub compared with the Mock- or GFP-expressing cells (Fig. 3A and B). Moreover, the D33A mutant-expressing cells did not show any signs of free di-Ub accumulation (Fig. 3A and B). In addition, lack of UCH-L3 expression in the tissues or MEF cells derived from Uchl3 knockout mice indicated no signs of di-Ub accumulation (Fig. 3C and data not shown). These results indicate that UCH-L3 does not function to hydrolyze free di-Ub.

3.4. Endogenous UCH-L3 does not show stabilizing effects on mono or di-Ub in cells or tissues

We have already shown that UCH-L1 interacts with and stabilizes mono-Ub *in vivo* (Osaka et al., 2003). The increased levels of free mono-Ub and di-Ub in the cells expressing WT and C95S mutant UCH-L3 in the immortalized 3T3 KO cells (Fig. 3A and B) prompted us to speculate that UCH-L3 might stabilize mono- and di-Ub *in vivo*. Thus, we compared the protein levels of mono- and di-Ub in various tissues from wild-type mice and knockout mice using Western blotting analysis with the anti-Ub antibody. As shown in Fig. 3C, tissues (including the testis where UCH-L3 expression is most abundant) of knockout mice did not show reduced mono-Ub or di-Ub levels. This result indicates that, at least in the tissues analyzed, UCH-L3 is not involved in the stabilization of di-Ub *in vivo*.

Please cite this article in press as: Setsuie, R., et al., Ubiquitin dimers control the hydrolase activity of UCH-L3. Neurochem. Int. (2009), doi:10.1016/j.neuint.2008.12.013

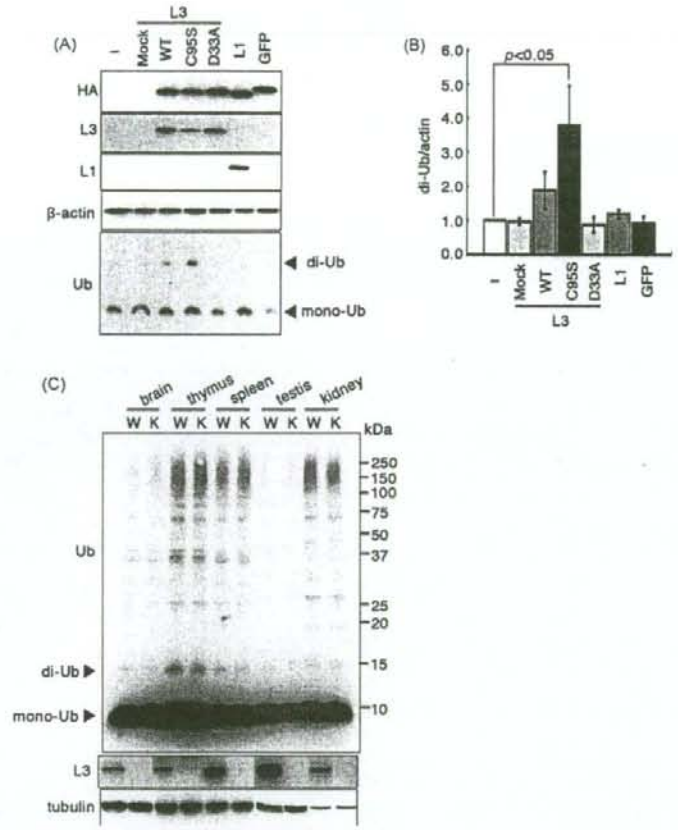

Fig. 3. UCH-L3 does not hydrolyze nor stabilize di-Ub *in vivo*. (A) The Western blotting analysis of immortalized MEF cells derived from Uchl3 knockout mice, which express FLAG-HA tagged UCH-L3 mutants. Note that these cells lack the expression of endogenous UCH-L3. (B) The quantitative analysis of bands corresponding to di-Ub in (A). The experiments were done three times and the statistical analysis was conducted by ANOVA followed by Dunnet's test. Data are mean ± S.E.M, $P < 0.05$. (C) Western blotting analysis of the tissues (whole brain, thymus, spleen, testis and kidney) from Uchl3 knockout (KO) mice and his wild-type littermate (WT) using anti-Ub antibody from Dako. Testis and spleen were included because these tissues express UCH-L3 most abundantly.

3.5. Di-Ub and mono-Ub inhibit the hydrolase activities of both UCH-L3 and UCH-L1

As shown in Fig. 2A and B, D33 and C95 of UCH-L3 are involved in the interaction with di-Ub. C95 is part of the active site triad of proteases and D33 is an essential amino acid for the interaction with Ub-aldehyde or Ub-vinylmethylsulfone (Wilkinson et al., 1999; Misaghi et al., 2005). Thus, we speculated that di-Ub might inhibit the enzymatic activity of UCH-L3. We performed *in vitro* hydrolase activity assays using Ub-AMC as the model substrate in the presence and absence of K48-linked, K63-linked and tandemly linked di-Ub and mono-Ub. As shown in Fig. 4A–C, the hydrolase activity of UCH-L3 is significantly inhibited in the presence of all forms of di-Ub and mono-Ub with the most prominent effect observed with the K48-linked di-Ub (about 60% inhibition). Meanwhile, mono-Ub as well as K48-linked di-Ub showed a significant inhibitory effect on the hydrolase activity of UCH-L1 (about 60% and 45% inhibition, respectively) (Fig. 4D).

4. Discussion

Our immunoaffinity purification assay coupled with LC–MS/MS analysis of Hela cells stably expressing exogenous UCH-L3 and UCH-L1 revealed that UCH-L3, but not its closest isozyme UCH-L1, interacts with di-Ub. Interaction with mono-Ub, an important physiological interacting partner of UCH-L1, was not observed with WT UCH-L3 in cells (Fig. 1). Structure analysis by X-ray crystallography and NMR spectroscopy indicated that important amino acids for the interaction of Ub-aldehyde or Ub-vinylmethylester, with UCH-L1 and UCH-L3 are all conserved in these two enzymes (Wilkinson et al., 1999; Misaghi et al., 2005). However, these enzymes share only 53% amino acid identity with different affinities for mono- and di-Ub (Figs. 1 and 2). In addition, the enzymatic activity toward the artificial Ub substrate (Ub-AMC) differs significantly between UCH-L1 and UCH-L3; UCH-L1 activity (Kcat) is less then 1/200 that of UCH-L3 (Liu et al., 2002). The amino acid sequences, which are not conserved among these UCHs should be responsible for these different characteristics.

Analysis of the UCH-L3 mutant revealed that D33 and C95 are essential for the interaction with di-Ub (Fig. 2). The previous kinetic analysis, NMR analysis and X-ray analysis revealed that C95 is an active site and D33 reside within the enzymatic catalytic pocket of UCH-L3 (Larsen et al., 1996; Johnston et al., 1997; Wilkinson et al., 1999; Misaghi et al., 2005). The carboxy terminal moiety of Ub in the ubiquitinated substrate penetrates this catalytic pocket of UCH-L3 and D33 of UCH-L3 forms a salt bridge

Please cite this article in press as: Setsuie, R., et al., Ubiquitin dimers control the hydrolase activity of UCH-L3. Neurochem. Int. (2009), doi:10.1016/j.neuint.2008.12.013

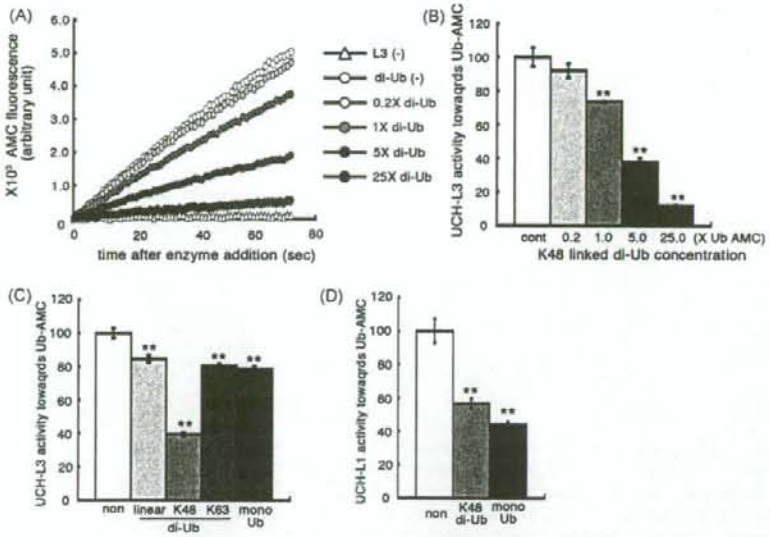

Fig. 4. Di-Ub inhibits UCH-L3 deubiquitinating activity while mono-Ub inhibits UCH-L1 deubiquitinating activity *in vitro*. (A) The kinetic curves of UCH-L3 in the presence or absence of K48-linked di-Ub. 0.2X or 1X or 5X or 25X moles of di-Ub compared to Ub-AMC substrate were included in the reaction. (B) The kinetic analysis of (A). (C) UCH-L3 deubiquitinating activity in the presence or absence of K48-linked or K63-linked or linear di-Ub or mono-Ub as in (B). 5X moles of di-Ub or mono-Ub compared to Ub-AMC substrate were included in the reaction. (D) UCH-L1 deubiquitinating activity in the presence or absence of K48-linked di-Ub or mono-Ub as in (B). 5X moles of di-Ub or mono-Ub compared to Ub-AMC substrate were included in the reaction. All statistical analyses were conducted by ANOVA followed by Dunnet's test. Data are mean ± S.E.M. ($n = 4$) $^{**}p < 0.001$ vs controls.

with R72 of Ub. The active site cysteine and an acidic residue corresponding to C95 and D33 of UCH-L3 are conserved among all UCH family proteins including UCH-L1 (Wilkinson et al., 1999; Misaghi et al., 2005). Thus, the interactions of di-Ub with UCH-L3 and mono-Ub with UCH-L1 occupy the catalytic centers of UCH-L3, and UCH-L1, respectively.

One of the physiological functions of UCH-L1 is to interact with mono-Ub and to protect mono-Ub from degradation (Osaka et al., 2003). This function was confirmed using *gad* mice and nm3419 mutant mice, which lack UCH-L1 protein expression. The protein level of free mono-Ub in the brain stem or the sciatic nerve, the site where *gad* mice are most severely affected, was prominently decreased in the *gad* mice compared with controls. In addition, cerebrum of nm3418 mutant mice also contained decreased levels of mono-Ub compared to that of control mice (Walters et al., 2008). Likewise, UCH-L3 might interact with di-Ub to protect it from degradation. To confirm this possibility, we compared the protein level of di-Ub in several tissues of UCH-L3 knockout mice with that of wild-type mice. In contrast with our expectations, none of the tissues derived from the knockout mice showed lower di-Ub levels (Fig. 3C). However, the exogenous expression of UCH-L3 in 3T3 immortalized mouse embryonic fibroblast, derived from the UCH-L3 knockout mice, revealed that its expression up-regulated the protein level of di-Ub, while the D33A mutant, a mutant that lacks the ability to interact with di-Ub, did not show this effect (Fig. 3A and B). Thus, we cannot exclude the possibility that, under some conditions, UCH-L3 may interact with di-Ub to protect it from degradation.

Previous biochemical analysis indicated that UCH-L3 is unable to hydrolyze tandemly conjugated di-Ub or K48-linked di-Ub (Larsen et al., 1998). To confirm that UCH-L3 is not capable of hydrolyzing di-Ub, we also performed *in vitro* enzymatic assays using K48-linked, and K63-linked di-Ub. We choose these two forms of di-Ub, among the eight possible linkages because these two forms of di-Ub are known to exist at relatively high levels *in vivo* (van Nocker and Vierstra, 1993; Hochstrasser, 2006). Consistent with the previous reports (Larsen et al., 1998), neither form of di-Ub was hydrolyzed by UCH-L3 even after 24 h incubation (data not shown). Thus, di-Ub is unlikely to be a substrate of UCH-L3.

Because the mutant analysis indicated that the catalytic pocket of UCH-L3 is affected by the interaction with di-Ub, another functional explanation of di-Ub interaction with UCH-L3 is that it might inhibit enzymatic activity. Indeed, the addition of K48-linked, K63-linked, and tandemly conjugated di-Ub, as well as mono-Ub showed inhibitory effects on hydrolyzing Ub-AMC (Fig. 4C). Of these three forms of di-Ub and mono-Ub, K48-linked di-Ub showed the most prominent inhibitory effect toward UCH-L3. A previous report indicated that nonhydrolyzable di-Ub analogues can inhibit Ub hydrolase activity of UCH-L3 where its activity was monitored by Ub-AMC (Yin et al., 2000). UCH-L3 was inhibited approximately equally by mono-Ub and di-Ub analogues linked through residues 11, 29, 48 (Kis of 200, 151, 199, and 107 μM, respectively) and the dimer analogue linked through residues 63 and 76 (head-to-head tandem conjugation) with a Ki of 13 μM (Yin et al., 2000). In addition, it has been reported that K48-linked di-Ub is the most abundant of all eight forms of di-Ub in tissues and cells. Thus, our results indicate that K48-linked di-Ub can function as an endogenous UCH-L3 inhibitor. Furthermore, we also found that addition of mono-Ub as well as K48-linked di-Ub inhibited the enzymatic activity of UCH-L1 (Fig. 4D). As UCH-L1 preferentially interacts with mono-Ub and the protein level of mono-Ub is high compared to di-Ubs in the cell, mono-Ub can function as endogenous inhibitor of UCH-L1. Together, these results indicate that di-Ub and mono-Ub regulate the enzymatic activity of UCH-L3 and UCH-L1, respectively.

In addition to Ub, UCH-L1 and UCH-L3 show affinity for Nedd8, an Ub-like protein, which shares 63% amino acid identity with Ub. Thus, these enzymes are thought to possess dual enzymatic activity toward the Ub and Nedd8 substrates. Although we could

Please cite this article in press as: Setsuie, R., et al., Ubiquitin dimers control the hydrolase activity of UCH-L3. Neurochem. Int. (2009), doi:10.1016/j.neuint.2008.12.013

not detect any types of Nedd8 derivatives in LC–MS/MS analysis, the Western blotting analysis of immunoaffinity-purified complexes with the Nedd8 specific antibody revealed several bands (Fig. 1D). The predicted molecular size of these bands indicates that UCH-L1 may interact with mono-Nedd8 while UCH-L3 may interact with di-Nedd8. UCHs are reported to show only weak affinity for Nedd8 compared with Ub. In addition, the expression level of Nedd8 protein is presumably low compared with that of Ub. These two differences might account for the limited amount of Nedd8 derivatives in the immunoaffinity-purified complex that can only be detected by Western blotting analysis. These interactions need to be further analyzed.

In conclusion, our analyses indicate that the major interacting partner of UCH-L1 is mono-Ub while that of UCH-L3 is di-Ub. These interactions appear to be responsible for the inhibition of deubiquitinating activity.

Acknowledgements

This work was supported by grants-in-aid for scientific research from the Japan Society for the Promotion of Science; a research grant in priority area research from the Ministry of Education, Culture, Sports, Science, and Technology, Japan; grants-in-aid for scientific research from the Ministry of Health, Labor, and Welfare, Japan; and the Program for Promotion of Fundamental Studies in Health Sciences of the National Institute of Biomedical Innovation and the New Energy and Industrial Technology Development Organization, Japan.

The authors thank Yoshihiro Nakatani and Hidesato Ogawa for providing the retroviral expression system and immunoaffinity purification system; Hiromi Fujita for the care and breeding of animals; Mari Suzuki, Yukihiro Tsuchiya, Tomohiro Kabuta and Yasuyuki Suzuki for valuable discussions.

References

Das, C., Hoang, Q.Q., Kreinbring, C.A., Luchansky, S.J., Meray, R.K., Ray, S.S., Lansbury, P.T., Ringe, D., Petsko, G.A., 2006. Structural basis for conformational plasticity of the Parkinson's disease-associated ubiquitin hydrolase UCH-L1. Proc. Natl. Acad. Sci. U. S. A. 103, 4675–4680.

Glickman, M.H., Ciechanover, A., 2002. The ubiquitin-proteasome proteolytic pathway: destruction for the sake of construction. Physiol. Rev. 82, 373–428.

Harada, T., Harada, C., Wang, Y.L., Osaka, H., Amanai, K., Tanaka, K., Takizawa, S., Setsuie, R., Sakurai, M., Sato, Y., Noda, M., Wada, K., 2004. Role of ubiquitin carboxy terminal hydrolase-L1 in neural cell apoptosis induced by ischemic retinal injury in vivo. Am. J. Pathol. 164, 59–64.

Hegde, A., Upadhya, S., 2007. The ubiquitin–proteasome pathway in health and disease of the nervous system. Trends Neurosci. 30, 587–595.

Hemelaar, J., Borodovsky, A., Kessler, B.M., Reverter, D., Cook, J., Kolli, N., Gan-Erdene, T., Wilkinson, K.D., Gill, G., Lima, C.D., Ploegh, H.L., Ovaa, H., 2004. Specific and covalent targeting of conjugating and deconjugating enzymes of ubiquitin-like proteins. Mol. Cell Biol. 24, 84–95.

Hershko, A., Ciechanover, A., 1998. The ubiquitin system. Annu. Rev. Biochem. 67, 425–479.

Hicke, L., 2001. Protein regulation by monoubiquitin. Nat. Rev. Mol. Cell Biol. 2, 195–201.

Hochstrasser, M., 2006. Lingering mysteries of ubiquitin-chain assembly. Cell 124, 27–34.

Johnston, S.C., Larsen, C.N., Cook, W.J., Wilkinson, K.D., Hill, C.P., 1997. Crystal structure of a deubiquitinating enzyme (human UCH-L3) at 1.8 A resolution. Embo J. 16, 3787–3796.

Kabuta, T., Setsuie, R., Mitsui, T., Kinugawa, A., Sakurai, M., Aoki, S., Uchida, K., Wada, K., 2008. Aberrant molecular properties shared by familial Parkinson's disease-associated mutant UCH-L1 and carbonyl-modified UCH-L1. Hum. Mol. Genet. 17, 1482–1496.

Kirisako, T., Kamei, K., Murata, S., Kato, M., Fukumoto, H., Kanie, M., Sano, S., Tokunaga, F., Tanaka, K., Iwai, K., 2006. A ubiquitin ligase complex assembles linear polyubiquitin chains. Embo J. 25, 4877–4887.

Kirkpatrick, D., Denison, C., Gygi, S., 2005. Weighing in on ubiquitin: the expanding role of mass-spectrometry-based proteomics. Nat. Cell Biol. 7, 750–757.

Kurihara, L.J., Kikuchi, T., Wada, K., Tilghman, S.M., 2001. Loss of Uch-L1 and Uch-L3 leads to neurodegeneration, posterior paralysis and dysphagia. Hum. Mol. Genet. 10, 1963–1970.

Kurihara, L.J., Semenova, E., Levorse, J.M., Tilghman, S.M., 2000. Expression and functional analysis of Uch-L3 during mouse development. Mol. Cell Biol. 20, 2498–2504.

Kwon, J., Wang, Y.L., Setsuie, R., Sekiguchi, S., Sakurai, M., Sato, Y., Lee, W.W., Ishii, Y., Kyuwa, S., Noda, M., Wada, K., Yoshikawa, Y., 2004. Developmental regulation of ubiquitin C-terminal hydrolase isozyme expression during spermatogenesis in mice. Biol. Reprod. 71, 515–521.

Larsen, C.N., Krantz, B.A., Wilkinson, K.D., 1998. Substrate specificity of deubiquitinating enzymes: ubiquitin C-terminal hydrolases. Biochemistry 37, 3358–3368.

Larsen, C.N., Price, J.S., Wilkinson, K.D., 1996. Substrate binding and catalysis by ubiquitin C-terminal hydrolases: identification of two active site residues. Biochemistry 35, 6735–6744.

Leroy, E., Boyer, R., Auburger, G., Leube, B., Ulm, G., Mezey, E., Harta, G., Brownstein, M.J., Jonnalagada, S., Chernova, T., Dehejia, A., Lavedan, C., Gasser, T., Steinbach, P.J., Wilkinson, K.D., Polymeropoulos, M.H., 1998. The ubiquitin pathway in Parkinson's disease. Nature 395, 451–452.

Liu, Y., Fallon, L., Lashuel, H.A., Liu, Z., Lansbury Jr., P.T., 2002. The UCH-L1 gene encodes two opposing enzymatic activities that affect alpha-synuclein degradation and Parkinson's disease susceptibility. Cell 111, 209–218.

Manago, Y., Kanahori, Y., Shimada, A., Sato, A., Amano, T., Sato-Sano, Y., Setsuie, R., Sakurai, M., Aoki, S., Wang, Y.L., Osaka, H., Wada, K., Noda, M., 2005. Potentiation of ATP-induced currents due to the activation of P2X receptors by ubiquitin carboxy-terminal hydrolase L1. J. Neurochem. 92, 1061–1072.

Misaghi, S., Galardy, P.J., Meester, W.J., Ovaa, H., Ploegh, H.L., Gaudet, R., 2005. Structure of the ubiquitin hydrolase UCH-L3 complexed with a suicide substrate. J. Biol. Chem. 280, 1512–1520.

Mukhopadhyay, D., Riezman, H., 2007. Proteasome-independent functions of ubiquitin in endocytosis and signaling. Science 315, 201–205.

Nijman, S.M., Luna-Vargas, M.P., Velds, A., Brummelkamp, T.R., Dirac, A.M., Sixma, T.K., Bernards, R., 2005. A genomic and functional inventory of deubiquitinating enzymes. Cell 123, 773–786.

Nishikawa, K., Li, H., Kawamura, R., Osaka, H., Wang, Y.L., Hara, Y., Hirokawa, T., Manago, Y., Amano, T., Noda, M., Aoki, S., Wada, K., 2003. Alterations of structure and hydrolase activity of parkinsonism-associated human ubiquitin carboxyl-terminal hydrolase L1 variants. Biochem. Biophys. Res. Commun. 304, 176–183.

Ogawa, H., Ishiguro, K., Gaubatz, S., Livingston, D.M., Nakatani, Y., 2002. A complex with chromatin modifiers that occupies E2F- and Myc-responsive genes in G0 cells. Science 296, 1132–1136.

Osaka, H., Wang, Y.L., Takada, K., Takizawa, S., Setsuie, R., Li, H., Sato, Y., Nishikawa, K., Sun, Y.J., Sakurai, M., Harada, T., Hara, Y., Kimura, I., Chiba, S., Namikawa, K., Kiyama, H., Noda, M., Aoki, S., Wada, K., 2003. Ubiquitin carboxy-terminal hydrolase L1 binds to and stabilizes monoubiquitin in neuron. Hum. Mol. Genet. 12, 1945–1958.

Rubinsztein, D.C., 2006. The roles of intracellular protein-degradation pathways in neurodegeneration. Nature 443, 780–786.

Saigoh, K., Wang, Y.L., Suh, J.G., Yamanishi, T., Sakai, Y., Kiyosawa, H., Harada, T., Ichihara, N., Wakana, S., Kikuchi, T., Wada, K., 1999. Intragenic deletion in the gene encoding ubiquitin carboxy-terminal hydrolase in gad mice. Nat. Genet. 23, 47–51.

Sakurai, M., Ayukawa, K., Setsuie, R., Nishikawa, K., Hara, Y., Ohashi, H., Nishimoto, M., Abe, T., Kudo, Y., Sekiguchi, M., Sato, Y., Aoki, S., Noda, M., Wada, K., 2006. Ubiquitin C-terminal hydrolase L1 regulates the morphology of neural progenitor cells and modulates their differentiation. J. Cell Sci. 119, 162–171.

Sakurai, M., Sekiguchi, M., Zushida, K., Yamada, K., Nagamine, S., Kabuta, T., Wada, K., 2008. Reduction in memory in passive avoidance learning, exploratory behaviour and synaptic plasticity in mice with a spontaneous deletion in the ubiquitin C-terminal hydrolase L1 gene. Eur. J. Neurosci. 27, 691–701.

Sano, Y., Furuta, A., Setsuie, R., Kikuchi, H., Wang, Y.L., Sakurai, M., Kwon, J., Noda, M., Wada, K., 2006. Photoreceptor cell apoptosis in the retinal degeneration of Uchl3-deficient mice. Am. J. Pathol. 169, 132–141.

Semenova, E., Wang, X., Jablonski, M.M., Levorse, J., Tilghman, S.M., 2003. An engineered 800 kilobase deletion of Uchl3 and Lmo7 on mouse chromosome 14 causes defects in viability, postnatal growth and degeneration of muscle and retina. Hum. Mol. Genet. 12, 1301–1312.

Setsuie, R., Wada, K., 2007. The functions of UCH-L1 and its relation to neurodegenerative diseases. Neurochem. Int. 51, 105–111.

Setsuie, R., Wang, Y.L., Mochizuki, H., Osaka, H., Hayakawa, H., Ichihara, N., Li, H., Furuta, A., Sano, Y., Sun, Y.J., Kwon, J., Kabuta, T., Yoshimi, K., Aoki, S., Mizuno, Y., Noda, M., Wada, K., 2007. Dopaminergic neuronal loss in transgenic mice expressing the Parkinson's disease-associated UCH-L1 I93M mutant. Neurochem. Int. 50, 119–129.

Todaro, G.J., Green, H., 1963. Quantitative studies of the growth of mouse embryo cells in culture and their development into established lines. J. Cell. Biol. 17, 299–313.

van Nocker, S., Vierstra, R.D., 1993. Multiubiquitin chains linked through lysine 48 are abundant in vivo and are competent intermediates in the ubiquitin proteolytic pathway. J. Biol. Chem. 268, 24766–24773.

Wada, H., Kito, K., Caskey, L.S., Yeh, E.T., Kamitani, T., 1998. Cleavage of the C-terminus of NEDD8 by UCH-L3. Biochem. Biophys. Res. Commun. 251, 688–692.

Walters, B., Campbell, S., Chen, P., Taylor, A., Schroeder, D., Dobrunz, L., Artavanistsakonas, K., Ploegh, H., Wilson, J., Cox, G., 2008. Differential effects of Usp14

Please cite this article in press as: Setsuie, R., et al., Ubiquitin dimers control the hydrolase activity of UCH-L3. Neurochem. Int. (2009), doi:10.1016/j.neuint.2008.12.013

and Uch-L1 on the ubiquitin proteasome system and synaptic activity. Mol. Cell. Neurosci. 45.
Wilkinson, K.D., 1997. Regulation of ubiquitin-dependent processes by deubiquitinating enzymes. Faseb J. 11, 1245–1256.
Wilkinson, K.D., Laleli-Sahin, E., Urbauer, J., Larsen, C.N., Shih, G.H., Haas, A.L., Walsh, S.T., Wand, A.J., 1999. The binding site for UCH-L3 on ubiquitin: mutagenesis and NMR studies on the complex between ubiquitin and UCH-L3. J. Mol. Biol. 291, 1067–1077.
Wilkinson, K.D., Lee, K.M., Deshpande, S., Duerksen-Hughes, P., Boss, J.M., Pohl, J., 1989. The neuron-specific protein PGP 9.5 is a ubiquitin carboxyl-terminal hydrolase. Science 246, 670–673.
Wood, M., Kaplan, M., Brensinger, C., Guo, W., Abel, T., 2005. Ubiquitin C-terminal hydrolase L3 (Uchl3) is involved in working memory. Hippocampus 15, 610–621.
Yin, L., Krantz, B., Russell, N.S., Deshpande, S., Wilkinson, K.D., 2000. Nonhydrolyzable diubiquitin analogues are inhibitors of ubiquitin conjugation and deconjugation. Biochemistry 39, 10001–10010.

Please cite this article in press as: Setsuie, R., et al., Ubiquitin dimers control the hydrolase activity of UCH-L3. Neurochem. Int. (2009), doi:10.1016/j.neuint.2008.12.013

Journal of
Nanoscience and Nanotechnology
Vol. 9, 670–672, 2009

Two-Photon Excitation Behavior of Thiophene-Based Oligomers and a Polymer

Takakazu Yamamoto[1,*], Akira Kumagai[1], Kenta Saito[2], and Takeharu Nagai[2,*]

[1] *Chemical Resources Laboratory, Tokyo Institute of Technology, 4259 Nagatsuta, Midori-ku, Yokohama 226-8503, Japan*
[2] *Research Institute for Electronic Science, Hokkaido University, Sapporo 001-0020, Japan*

The two-photon excitation action cross-sections of four kinds of co-oligomers of thiophene and pyridine (e.g., Py-$(Th)_n$-Py; Py = 2-pyridyl, Th = thiophene-2,5-diyl; $n = 3$, 4) and a copolymer constituted of alternating pyridazine and 4,4′-dihexyl- 2,2′-bithiophene units have been measured by using a reported value (σ_{2PE} at 780 nm = 10 GM) of green fluorescent protein as the reference. The co-oligomers give σ_{2PE} values of 14–26 GM and the copolymer shows σ_{2PE} of 23 GM.

Keywords: π-Conjugated Polymer, Oligomer, Two-Photone Excitation.

Two-photon absorption phenomena are the subject of recent many papers.[1–8] One of the important applications is two-photon excitation of fluorescent molecules within deep inside living tissue. In combination with FRET (fluorescence resonance energy transfer)-based indicators, protein–protein interactions and activities of biomolecules are visualized.[8,9] Another application is the use as a light source for micro-fabrication to make, for example, three dimensional photonic crystals.[10] By the way, π-conjugated oligomers and polymers are also the subject of recent interest,[11–14] and two-photon absorption data of π-conjugated oligomers and polymers are expected to give information about fundamental electronic states of the oligomers and polymers.

Recently we reported synthesis of the following π-conjugated co-oligomers and copolymer[15,16] with an intramolecular charge transferred (CT) electronic structure. In the co-oligomers and copolymer, thiophene is an electron-donating unit, whereas pyridine and pyridazine are electron-accepting units.[15,16] For these co-oligomers and copolymer we have studied their two-photon absorption behavior.

We herein report the obtained results. The two-photon absorption data were acquired by irradiation of solutions of the co-oligomers and copolymer with 780 nm laser. According to the one photon absorption spectrum of the tested dyes, we used 780 nm laser as the light source for two-photon excitation.

The co-oligomers **1–6** (Ref. [15]) and the copolymer P(PydTh) (R = hexyl)[16] were prepared according to the literature. α-Sexithiophene (α-Th_6) was purchased from Tokyo Kasei Co. Ltd. Fluorescence spectra were recorded on a Hitachi F-4010 spectrometer. Quantum yield (Φ) of fluorescence was calculated using a quinine sulfate standard (ca. 10^{-5} M solution in 0.5 M H_2SO_4 with $\Phi = 54.6\%$[17]). Two-photon excitation was carried out under an inverted microscopy (Olympus FV-300) equipped with an Olympus 20× NA0.75 objective lens. 780 nm pulse laser (Maitai, Spectra Physics) was irradiated to the sample solution in the two-photon excitation, and intensity of the laser was adjusted by a computer controlled AOTF (acousto-optical tunable filter) system. Fluorescence intensity in a region of interest was measured. Florescence intensity of pure chloroform did not show dependence on the intensity of the laser. mSEGFP, a variant of green fluorescent protein with mutations in EGFP (M153T, V163A, S175G and A206K), was used as the standard for determination of the cross section (σ_{2PE}) of the two-photon absorption (σ_{2PE} of mSEGFP = 10 GM (1 GM = 10^{-50} cm^4 s/photon)[7,18]). Co-oligomers **1–6** were dissolved in DMSO (dimethyl sulfoxide), and P(PydTh) (6.5 mg) was dissolved in 8.0 mL of xylene at 100 °C. Most part of P(PydTh) was dissolved in xylene, however, there was some insoluble part. The insoluble part was removed by filtration.

Figure 1 shows dependence of the fluorescence intensity of the co-oligomers **3–6** and α-Th_6 on the intensity of irradiated laser at 780 nm. Solutions of these co-oligomers and α-Th_6 show the UV-vis absorption peak in a range of about 380–440 nm,[15] and they are essentially transparent at 780 nm. The co-oligomers 1 and 2 with a shorter

*Authors to whom correspondence should be addressed.

1533-4880/2009/9/670/003 doi:10.1166/jnn.2009.J070

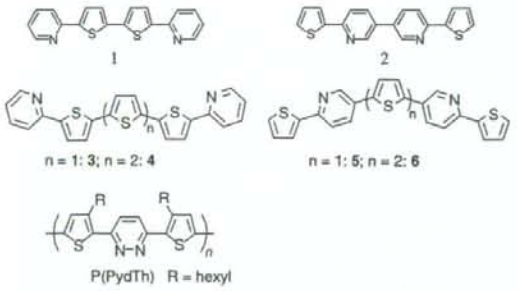

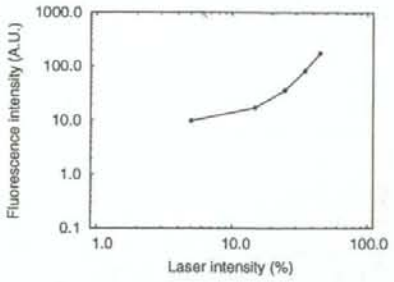

Fig. 2. Dependence of fluorescence intensity on the laser intensity at 780 nm. Data for the co-oligomer **1** in chloroform.

π-conjugation length did no show strong dependence of the fluorescence intensity on the laser intensity when the laser intensity is not strong (e.g., cf. data shown in Fig. 2 for the co-oligomer 1). This suggests that 1 and 2 were not so active for the two-photon excitation. The shorter π-conjugation system may not be suited for an effective two-photon excitation. However, when the laser intensity becomes stronger, the fluorescence shows nonlinear increase by increasing the laser intensity and the final slope of the curve seems to be larger than the average slopes in the figures in Figure 1. The reason for the larger slope in the region of the strong laser intensity and the small slope in the region of weaker laser intensity is not clear, however, the results suggest contribution of higher-order multi-photon absorption at strong laser intensity, and further detailed examination of the phenomenon is expected to reveal the origin of the nonlinear behavior.

As shown in Figure 1, co-oligomers **3–6** with a longer π-conjugation system and the intramolecular CT electronic structure show a strong linear relationship between the laser intensity and the fluorescence intensity in logarithm scales, indicating that they are active for the two-photon excitation. The intensity of the fluorescence increases roughly linearly with (laser intensity).[2] The copolymer P(PydTh) also shows a strong dependence of fluorescence on the laser intensity as shown in Figure 3.

The cross section (σ_{2PE}) of the two-photon absorption was determined for the co-oligomers **3–6** and P(PydTh) from the data exhibited in Figures 1 and 3, and the data are shown in Table I. The UV-vis peak positions (λ_{max}) and the cut-off positions of the co-oligomers and polymer are also shown in Table I. As shown in Table I, the co-oligomers **3–6** and P(PydTh) give larger σ_{2PE}'s than those of mSEGFP used as the standard. σ_{2PE} of α-Th_6 was also estimated under the same conditions as shown in Table I, and the estimated value is considerably smaller than those of the co-oliogmers **3–6**, although α-Th_6 has a π-conjugation length similar to those of the co-oligomers **3–6**. The much larger σ_{2PE}'s of the co-oligomers **3–6** than that of α-Th_6 suggest an important contribution of the CT electronic structure of the co-oligomers **3–6** to σ_{2PE}.

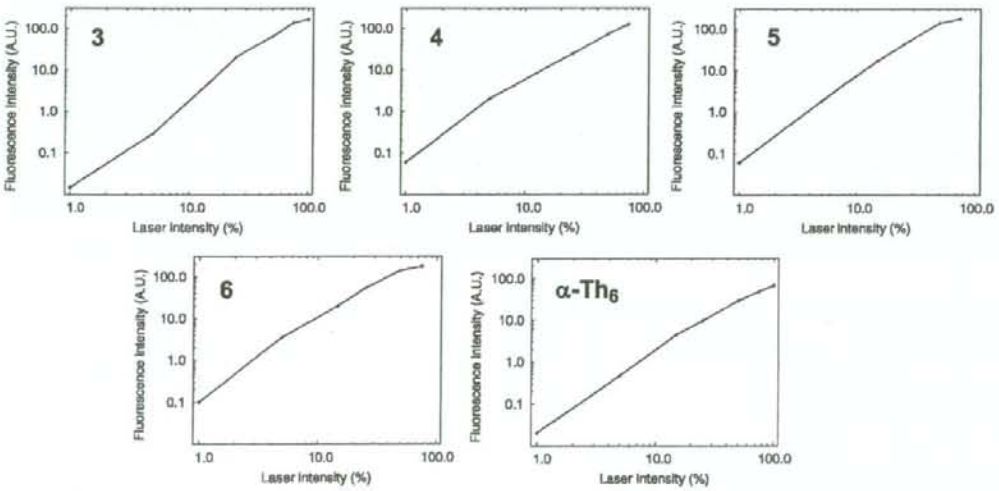

Fig. 1. Dependence of fluorescence intensity on the laser intensity at 780 nm. Data obtained with the co-oligomers **3–6** in dimethyl sulfoxide. Fluorescence intensity is given in an arbitrary unit.

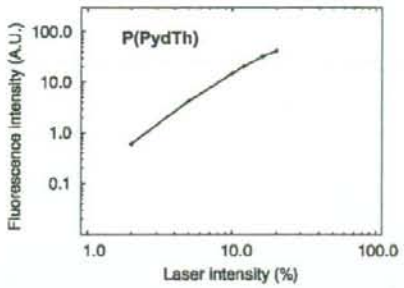

Fig. 3. Dependence of fluorescence intensity of P(PydTh) in xylene.

Table I. Fluorescence quantum yield, Φ, and cross section, σ_{2PE}, of the two-photon absorption of the co-oligomers **3–6** and copolymer P(PydTh).[a]

Sample	c (M)	Φ	σ_{2PE} at 780 nm (GM)	λ_{max} (nm)	Cut-off (nm)
mSEGFP	6.6×10^{-5}	0.6	10		
3	1.1×10^{-4}	0.21	24	418	475
4	0.7×10^{-4}	0.35	26	435	505
5	1.5×10^{-4}	0.33	23	384	470
6	2.8×10^{-4}	0.37	14	408	480
P(PydTh)	3.9×10^{-5}	0.59	23	449	530
α-Th_6	9.6×10^{-4}	0.3	1.1	432	520

[a]Concentration of P(PydTh) is based on the repeating unit of the copolymer.

P(PydTh) showed a σ_{2PE} value comparable to those of the co-oligomers **3–6**, suggesting that the π-conjugation length composed of 5 or 6 aromatic units was enough for the two-photon excitation by the CT-type compounds. The obtained results and further detailed studies based on the two-photon excitation behavior of π-conjugated molecules and polymers are expected to give better understanding of electronic state of the π-conjugated molecules and polymers.

Acknowledgments: We are grateful to Professor H. Fukumoto and Dr. T. Yasuda of Tokyo Institute of Technology and Dr. Tomoki Matsuda of Hokkaido University for their experimental supports. This research was partly supported by a Grant-in-Aid for Science Research in Priority Area "Super-Hierarchical Structures" and Special Education and Research Expenses for "Post-Silicon Materials and Devices Research Alliance" from the Ministry of Education, Culture, Sports, Science, and Technology, Japan.

References and Notes

1. M. Albota, D. Beljonne, J.-L. Brédas, J. E. Ehrlich, J.-Y. Fu, A. A. Heikal, S. E. Hess, T. Kogej, M. D. Levin, S. R. Marder, D. McCord-Maughon, J. W. Perry, H. Röckel, M. Rumi, G. Subramaniam, W. W. Web, X.-L. Wu, and C. Xu, *Science* 281, 1653 (**1998**).
2. B. Cumpston, S. P. Ananthavel, S. Barlow, D. L. Dyer, J. Ehrlich, L. L Erskine, A. A. Heikal, S. M. Kuebler, I.-Y. S. Lee, D. McCord-Maughon, J. Qin, H. Röckel, M. Rumi, X.-L. Wu, S. R. Marder, and J. W. Perry, *Nature* 398, 51 (**1999**).
3. F. Stabo-Eeg, M. Lindgren, P. R. Nilsson, O. Inganäs, and P. Hammarström, *Chem. Phys.* 336, 121 (**2007**).
4. M. Shimizu, M. Schelper, K. Mochida, T. Hiyama, M. Adachi, Y. Sasaki, S. Akiyama, S. Maeda, H. Kanbara, Y. Mori, and T. Kurihara, *Adv. Mater.* 19, 1826 (**2007**).
5. N. Pfeffer, P. Raimond, F. Charra, and J.-M. Nunzi, *Chem. Phys. Lett.* 201, 357 (**1993**).
6. H. Ohkita and S. Ito, *Kokagaku* 31, 84 (**2000**); *Chem. Abstr.* 135, 377757v (**2001**).
7. G. A. Blab, P. H. M. Lommerse, L. Cognet, G. S. Harms, and T. Schmidt, *Chem. Phys. Lett.* 350, 71 (**2001**).
8. K. Okamoto, T. Nagai, A. Miyawaki, and Y. Hayashi, *Nat. Neurosci.* 7, 1104 (**2004**).
9. K. Takao, K. I. Okamoto, T. Nakagawa, R. L. Neve, T. Nagai, A. Miyawaki, T. Hashikawa, S. Kobayashi, and Y. Hayashi, *J. Neurosci.* 25, 3107 (**2005**).
10. H. B. Sun, S. Matsuo, and H. Misawa, *Appl. Phys. Lett.* 74, 786 (**1999**).
11. H. S. Nalwa, Handbook of Organic Conductive Molecules and Polymers, John Wiley, Chichester (**1997**).
12. T. A. Skotheim, R. L. Elsembaumer, and J. R. Reynolds, Handbook of Conducting Polymers, 2nd edn., Marcel Dekker, New York (**1997**).
13. T. A. Skotheim and J. R. Reynolds, Handbook of Conducting Polymers, 3rd edn., CRC Press, Boca Raton, Florida (**2007**).
14. S. Hotta, Electronic and Optical Properties of Conjugated Molecular Systems in Conjugated Phases, Research Signopost, Kerala (**2003**).
15. H. Fukumoto, A. Kumagai, Y. Fujiwara, H. Koinuma, and T. Yamamoto, *Heterocycles* 68, 1349 (**2006**).
16. T. Yasuda, Y. Sasaki, S. Aramaki, and T. Yamamoto, *Chem. Mater.* 17, 6060 (**2005**).
17. W. H. Melhuish, *J. Phys. Chem.* 64, 762 (**1960**).
18. M. A. Albota, C. Xu, and W. W. Webb, *Appl. Optics* 37, 7352 (**1998**).

Received: 28 December 2007. Accepted: 15 February 2008.

COMMUNICATION

CELL STRUCTURE AND FUNCTION 33: 133–141 (2008)

A Mercury Arc Lamp-Based Multi-Color Confocal Real Time Imaging System for Cellular Structure and Function

Kenta Saito[1], Kentaro Kobayashi[1], Tomomi Tani[2], and Takeharu Nagai[1,2]*

[1]Nikon imaging center, Research Institute for Electronic Science, Hokkaido University, N20 W10 Kita-ku, Sapporo, Hokkaido, 001-0020, Japan, and [2]Laboratory for Nanosystems Physiology, Research Institute for Electronic Science, Hokkaido University, N20 W10 Kita-ku, Sapporo, Hokkaido, 001-0020, Japan

ABSTRACT. **Multi-point scanning confocal microscopy using a Nipkow disk enables the acquisition of fluorescent images with high spatial and temporal resolutions. Like other single-point scanning confocal systems that use Galvano meter mirrors, a commercially available Nipkow spinning disk confocal unit, Yokogawa CSU10, requires lasers as the excitation light source. The choice of fluorescent dyes is strongly restricted, however, because only a limited number of laser lines can be introduced into a single confocal system. To overcome this problem, we developed an illumination system in which light from a mercury arc lamp is scrambled to make homogeneous light by passing it through a multi-mode optical fiber. This illumination system provides incoherent light with continuous wavelengths, enabling the observation of a wide range of fluorophores. Using this optical system, we demonstrate both the high-speed imaging (up to 100 Hz) of intracellular Ca^{2+} propagation, and the multi-color imaging of Ca^{2+} and PKC-γ dynamics in living cells.**

Key words: confocal microscopy/live imaging/laser/arc lamp/Nipkow disk

Introduction

Laser-scanning confocal microscopy has been a method of choice for examining biological structures at the sub-cellular, cellular, and tissue levels in three dimensions for several decades, due to its ability to acquire images of thin optical sections within thick samples (Swedlow *et al.*, 2004; Hibbs, 2004). However, a single-point scanning system usually takes several seconds to scan a single viewing field, which is a disadvantage for real-time imaging. Thus, multi-point scanning confocal systems using a scanning disk have been developed to achieve high-speed imaging without losing spatial resolution (Ichihara *et al.*, 1996). The Yokogawa CSU10 is well known as one of the most advanced scanning disk systems. In this system, an expanded laser beam is directed onto a Nipkow disk, which contains arrays made up of tandem pairs of microlenses and pinholes, arranged circumferentially at a constant angle and radially at constantly decreasing distances from the center. When the disk is spun, each microlens/pinhole pair sweeps the excitation laser beam across the object through the objective lens, producing a raster scan of multiple laser beams. This scanning system provides two advantages for confocal imaging: 1) a faster frame acquisition rate (up to 360 Hz) because of the simultaneous scanning by approximately 1200 points, and 2) a reduction of photo-induced damage, because the excitation light power of each scanning point can be reduced to as low as 1/1200 of that of the single-point scanning system (Inoué and Inoué, 2002; Wang *et al.*, 2005). There are some other commercially available disk-scanning systems with pinholes/slits, but they are different from the Yokogawa CSU10. The Olympus DSU employs a scanning disk with silts, which allows the acquisition of quasi-confocal images; however, there is no confocal effect along the horizontal aperture of the slit. The CARV II (BD Bioscience) has a Nipkow disk with pinholes, but the pinholes are larger (CARV II; 70 mm, CSU10; 50 mm), which reduces the confocal effect. Therefore, the axial resolution for both of these systems is lower than for the CSU10 (Toomre and Pawley, 2006).

As the excitation light source, visible wavelength lasers (Argon ion, Krypton-argon ion, Helium-neon ion, and other

*To whom correspondence should be addressed: Takeharu Nagai, Laboratory for Nanosystems Physiology, Research Institute for Electronic Science, Hokkaido University, N20 W10 Kita-ku, Sapporo, Hokkaido, 001-0020, Japan.
Tel: +81-11-706-9438, Fax: +81-11-706-9443
E-mail: tnagai@es.hokudai.ac.jp

Abbreviations: FWHM, Full-width at the half-maximal intensity; OGB, Oregon Green-488 BAPTA-1; PKC-γ, protein kinase C-γ; YC3.60, yellow cameleon 3.60.

solid-state visible lasers) have been used for both single-point and multiple-point scanning confocal systems. However, the use of lasers often limits the choice of fluorescent dyes to be excited, because irradiated laser lights contain a relatively narrow range of wavelengths. Moreover, the use of coherent laser light with a Nipkow-disk confocal system generally results in considerable degradation of the image (Fewer *et al.*, 1998). In contrast to a laser light source, a mercury arc lamp provides incoherent light with a much broader range of wavelengths, from 250 nm to 600 nm, and is commonly used as an excitation light source for conventional wide-field fluorescent microscopes. At a certain wavelength, the axial or lateral resolution of a confocal microscope is determined primarily by the size of the pinhole and the performance of the objective and tube lenses. Thus, confocal-based optical sectioning is possible, regardless of the excitation light source. Based on the idea that the mercury arc lamp provides a much broader range of wavelengths than a laser, illumination with a mercury arc lamp would be preferable for a Nipkow disk confocal system. In spite of this, there has been no report of applying a mercury arc lamp as the light source for the Yokogawa CSU system, possibly due to the difficulty of obtaining intense and uniform illumination of the specimen.

Here we report a method for multiple-point scanning confocal microscopy using a 100 W mercury arc lamp as the light source. In this system, a large diameter (~1 mm in diameter) multi-mode optical fiber is inserted between the arc lamp and the confocal system, providing stable, intense, and uniform illumination. The excitation wavelength is determined by filter selection, as in conventional wide field epi-fluorescence microscopy systems. This microscopy system enables the visualization of multiple-molecular dynamics in living cells without limiting the choice of fluorophores. Using this system, we show both high-speed (up to 100 Hz) and multiple color confocal imaging of dynamic biological events. In addition, we discuss other suitable applications for this new, convenient confocal system.

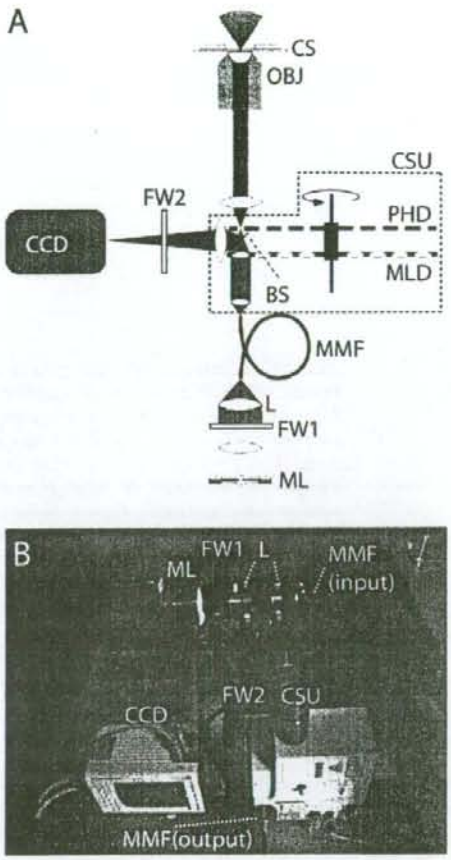

Fig. 1. Nipkow disk confocal unit with mercury arc lamp illumination system. (A) A schematic diagram of the Nipkow disk confocal unit with mercury arc lamp illumination system. ML: 100 W mercury arc lamp, FW1: Filter wheel for excitation, L: collection lens, MMF: multi-mode optical fiber, BS: beam splitter, CSU: Yokogawa CSU10, MLD: microlens array Nipkow disk, PHD: pinhole array Nipkow disk, OBJ: objective lens, CS: cover slip and sample, FW2: filter wheel for emission, CCD: cooled CCD camera. (B) Photograph of the Nipkow disk confocal unit with mercury arc lamp illumination system.

Materials and Methods

Nipkow disk confocal unit with mercury arc lamp illumination system

Fig. 1 shows a schematic diagram of the Nipkow disk confocal unit with a mercury arc lamp illumination system. The system consists of an inverted microscope (TE2000-E, Nikon, Tokyo, Japan) and a commercially available Nipkow disk confocal unit (CSU10, Yokogawa Electric, Tokyo, Japan). A 60×, or 100× PlanApo NA1.4 oil-immersion objective lens (Nikon, Tokyo, Japan) was used to collect the images. The light from a 100 W mercury arc lamp was focused onto the input end (1.0 mm in diameter) of a multi-mode optical fiber (ST1000H; Mitsubishi Electric Cable, Tokyo, Japan) to scramble the light (Kam *et al.*, 1993; Tani *et al.*, 2005). The light from the fiber's output end was then directed to the CSU10. A MAC 5000 system (Ludl, Hawthorne, NY) was used to control the filter wheels for the excitation and emission light and for shuttering the excitation light. The emitted light collected by the objective lens was focused on a cooled electron-multiplying charge-coupled device (EM-CCD) camera (ImagEM; Hamamatsu Photonics, Hamamatsu, Japan) or a cooled 3CCD camera (ORCA-3CCD; Hamamatsu Photonics). The shutter, filter

wheels, and camera were controlled by the software, AquaCosmos version 2.6 (Hamamatsu Photonics).

Spatial resolution measurements

To compare the spatial resolution of a confocal system using a mercury arc lamp with that using an Ar^+ laser, 0.1 μm-diameter fluorescent beads (TetraSpeck; Molecular Probes, Eugene, OR) were used. Excitation light through a mercury arc lamp with a 470/40 nm excitation filter or a 488-nm Ar^+ laser (20 mW; model 532-BS-A04; Melles Griot, Carlsbad, CA) was used to collect images of the beads. Six images obtained using each excitation light were averaged and compared.

Cell preparation

HeLa cells were cultured in homemade 35-mm glass-bottomed dishes in Dulbecco's modified Eagle's medium (DMEM; Sigma, St. Louis MO) containing 10% fetal bovine serum (BioWest, Nuaillé, France). The cells were transfected with plasmids using Lipofectamine 2000 (Invitrogen, Carlsbad, CA). The transfected cells were cultured for 1 to 2 days before observation.

Gene construction

The DNA sequence encoding the N-terminal 12 amino acids of cytochrome *c* oxidase subunit IV (CoxIV) was fused to the sequence encoding the N-terminus of mSECFP (Matsuda *et al.*, 2008), to obtain mSECFP-mit, which specifically localizes to the mitochondrial matrix. The nuclear localization signal sequence (NLS) of SV40 large T-antigen was fused to the C-terminus of mRFP1 (Campbell *et al.*, 2002) to obtain mRFP1-nu, which localizes to the nucleus. mSECFP-er was generated by extending the N-terminus of mSECFP with the signal peptide sequence of calreticulin and the C terminus of mSECFP with the ER retention signal sequence KDEL, which localizes to the endoplasmic reticulum. The sequences encoding mSECFP, mSECFP-mit, mRFP1-nu, and mSECFP-er were cloned into the pcDNA3 vector (Invitrogen, Carlsbad, CA). Venus-Actin was generated by replacing the EYFP gene of pEYFP-Actin (Clontech Laboratories, Palo Alto, CA) with the Venus gene (Nagai *et al.*, 2002). The DsRed1 gene of pPKC-γ-DsRed1 (Clontech Laboratories) was replaced with the gene for its rapidly maturating variant, DsRed T3 (Bevis and Benjamin, 2002) to construct PKC-γ-DsRed T3. The construction of yellow cameleon 3.60 (YC3.60) was reported previously (Nagai *et al.*, 2004).

High-speed [Ca^{2+}] imaging

HeLa cells were incubated in DMEM containing 5 μM Oregon Green-488 BAPTA-1 AM (Molecular Probes, Eugene, OR) for 1 hour at room temperature, washed twice with PBS, and transferred to DMEM again before observation. A 470/40 nm filter (Nikon, Tokyo, Japan) was used as the excitation filter. To show the spatial propagation of the Ca^{2+} wave clearly, the obtained images were

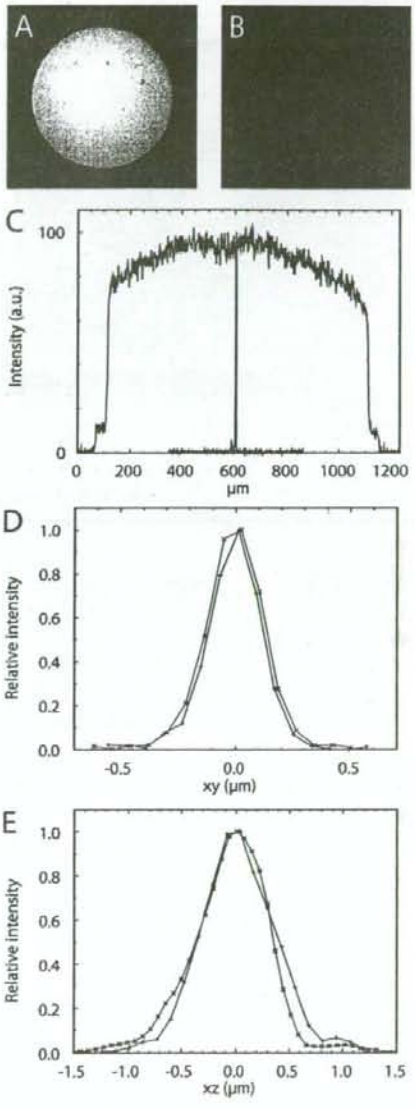

Fig. 2. Comparison of the efficiency of the CSU10 with mercury arc lamp versus 488-nm Ar^+ laser. (A and B) Images of the optical fiber output end coupled to a mercury arc lamp (A) or 488-nm Ar^+ laser (B). (C) The intensity profiles across the center of the images in A (red line) and B (green line), normalized to the peak intensity. (D, E) The spatial resolution of the CSU10 with mercury arc lamp (red line) and 488-nm Ar^+ laser (green line). (D) Horizontal intensity profiles across just the middle section of stacks of a 0.1-μm fluorescent bead. (E) Vertical intensity profiles across the center of a 0.1-μm fluorescent bead.

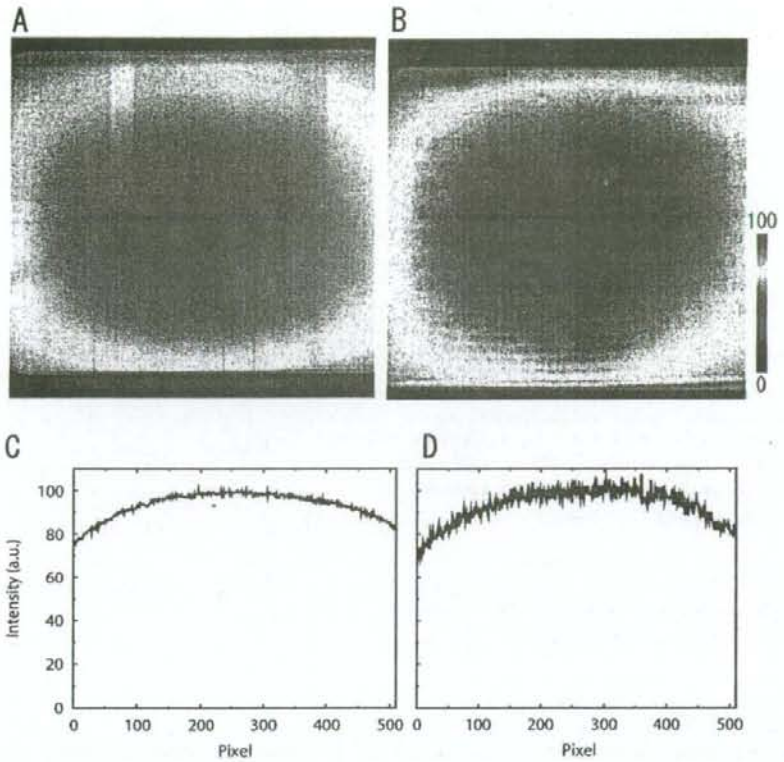

Fig. 3. The uniformity of illumination on a sample. (A and B) The images of a fluorescent plate obtained using the CSU10 with illumination from a mercury arc lamp (A) or 488-nm Ar^+ laser (B). (C and D) The normalized intensity profiles across the center of the images in A (C) and B (D).

smoothed by taking the rolling average over 4 images. From the series of fluorescent images, the relative change in the intracellular Ca^{2+} was calculated from the fluorescence intensity value (F) of the cell divided by its value at time 0 (F_0). The obtained changes in F/F_0 were shown as a series of pseudo-color images.

Multi-color imaging using a half-reflective mirror

For multi-color imaging, we used a half-reflective mirror, T50 (Asahi-spectra Co., Tokyo, Japan), that transmits approximately 50% of visible wavelengths from 400 nm to 700 nm. We used the following combination of excitation and emission filters, respectively: 440/21 nm and 480/30 nm for mSECFP, 490/20 nm and 535/26 nm for Venus, and 540/30 nm and 575 nm long path filter for mRFP1 (all filters were from Omega Optical and are designated by the central wavelengths of their transmittance and band widths at half-maximal transmittance). For the multi-color time-lapse imaging of HeLa cells expressing both YC3.60 and PKC-γ-DsRed T3, we used 440/21 nm and 540/30 nm for YC3.60 and DsRed T3 excitation, respectively, and 480/30 nm, 535/26 nm, and 575 nm long pass filter for mSECFP, Venus, and DsRed T3 emission, respectively. All of the excitation and emission filters were automatically alternated by filter wheels, using the MAC 5000 system (Ludl, Hawthorne, NY).

Results and Discussion

Comparison of illumination at the ends of the optical fiber and spatial resolution using different light sources

A Nipkow disk confocal microscope requires an illumination system that provides uniform excitation light for each scanning point. To obtain uniform illumination from a mercury arc lamp, we introduced a multi-mode, large diameter (1 mm) optical fiber into the illumination system as a light scrambler (Fig. 1A). Typical images of the output end of the multi-mode optical fiber coupled to a mercury arc lamp and

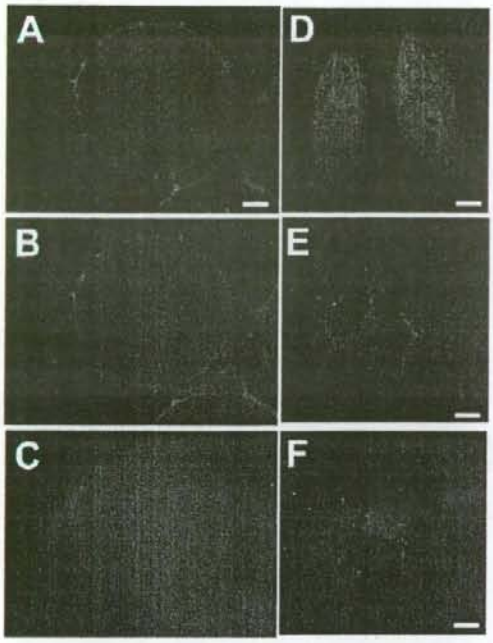

Fig. 4. Optical sectioning of biological samples. (A–C) Real-color images of confocal or non-confocal optical sections of a pumpkin pollen grain. These images were obtained by the CSU10 with a mercury arc lamp (A) or 488-nm Ar^+ laser (B) or by non-confocal (wide field) fluorescence microscopy (C). Scale bar represents 20 μm. (D–F) Images of HeLa cells expressing mSECFP in the cytoplasm and the nucleus (D), mSECFP in the endoplasmic reticulum (E), and mSECFP in the mitochondria (F). Scale bar represents 10 μm.

that of a single-mode optical fiber coupled to a 488-nm Ar^+ laser are shown in Fig. 2A and B, respectively. The intensity profile of the image obtained from the multi-mode fiber output is shown in Fig. 2C. The light was uniformly distributed, and did not reflect the image of the mercury arc's geometry.

The excitation light from the output end of a multi-mode or single-mode fiber end was then introduced into the CSU10 Nipkow disk-type confocal scanner unit. To compare quantitatively the spatial resolution of the system using a mercury arc lamp with that using a 488-nm Ar^+ laser line, we collected three-dimensional images of a 0.1-μm fluorescent bead. The intensity profiles of the images along the X-axis and Z-axis are shown in Fig. 2D and E, respectively. The full width at half-maximal intensity (FWHM) of the images in the xy plane was 0.27 μm for the mercury arc lamp and 0.24 μm for the 488-nm Ar^+ laser (Fig. 2D). The FWHM of the bead image on the xz plane was 0.76 μm for the mercury arc lamp and 0.72 μm for the laser light (Fig. 2E). These results indicate no significant differences in the point-spread function on the xy and xz planes between a CSU10 disk illuminated with a mercury arc lamp versus a 488-nm Ar^+ laser. Thus, the mercury arc lamp illumination was equivalent to the 488-nm Ar^+ laser for acquiring confocal images through the CSU10.

The power and uniformity of illumination

We measured the power of the excitation light of the mercury arc lamp at the input and output ends of the multi-mode optical fiber and at the level of the specimen. With a 470/40 nm band-pass filter, the power at these levels was 60, 8, and 0.05 mW, and with a 540/30 nm band-pass filter, it was 150, 30, and 0.19 mW, respectively. The power of the excitation light with the 470/40 nm filter was lower than that with the 540/30 nm filter, because the mercury arc lamp has prominent emission lines in 540/30 nm but not in 470/40 nm. The applicability of excitation light with no prominent emission line to high-speed imaging will be examined later in this article.

To examine the uniformity of illumination on the specimen, we obtained an image of a fluorescent plate filled with uniformly distributed fluorescent dyes. With both the mercury arc lamp (Fig. 3A) and the 488-nm Ar^+ laser light (Fig. 3B), the peak of intensity was at the center of the image, and about a 20% decrease in signal was seen at the periphery of the image (Fig. 3C, D). In spite of the large difference in the intensity profile at the end of the optical fiber (Fig. 2A–C), there was no significant difference in the uniformity of illumination on the specimen between the mercury arc lamp and the 488-nm Ar^+ laser.

Optical sectioning of biological samples

For further demonstration of the use of the mercury arc lamp as an ideal light source for CSU10, we took confocal fluorescent images of pumpkin pollen grains (diameter, ~100 μm), a useful sample for testing the effect of optical sectioning by confocal systems using a mercury arc lamp (Fig. 4A) and 488-nm Ar^+ laser (Fig. 4B). As a comparison, the same image was taken with a wide-field microscope (Fig. 4C). There was no significant difference between the images obtained using the mercury arc lamp versus the laser (Fig. 4A, B) whereas in the image taken by wide-field microscopy, the inside structure of the pumpkin pollen grain was unclear and the background fluorescence was higher (Fig. 4C) than in the confocal images. Thus, it was fully expected that optical sections of even a single living HeLa cell (~10 μm thickness) might be obtained with the CSU10 with mercury arc lamp system. To verify this, we visualized mSECFP localized to specific organelles in HeLa cells using the CSU10 with a mercury arc lamp as a light source. The condensed structures (vesicles, nucleolus) inside the cell contrasted well with the mSECFP in the cytoplasm and

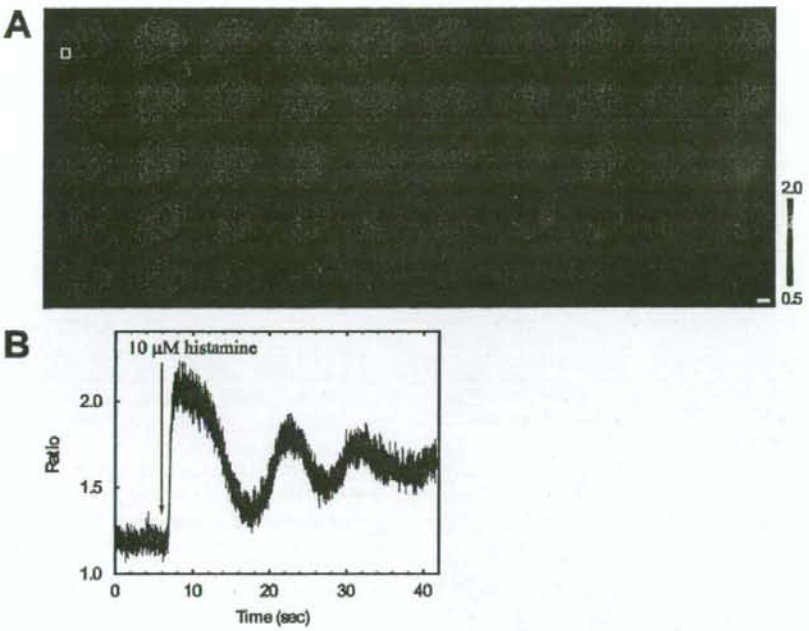

Fig. 5. High-speed confocal Ca^{2+} imaging by the CSU10 with mercury arc lamp. (A) A series of pseudo-colored images of HeLa cells loaded with Oregon Green-488 BAPTA-1 AM. Scale bar represents 10 μm. (B) Time course of the F/F_0 ratio value at the ROI indicated in (A).

the nucleus (Fig. 4D), and the network structure of the endoplasmic reticulum (Fig. 4E), and the tubule structure of the mitochondria (Fig. 4F) were clearly seen. In wide-field microscopy, these structures cannot be seen clearly because of high background fluorescence from the out-of-focus planes.

High-speed confocal imaging with excitation illumination by mercury arc lamp

The mercury arc lamp has several prominent emission lines, at 366, 405, 435, 546, and 578 nm, with peak intensities up to 6–10 times higher than the average intensity of the residual emission wavelength. These prominent emission lines can be used to easily excite fluorescent dyes such as DAPI, CFP, DsRed, and mRFP1 effectively. However, there are no prominent emission lines between 450 nm and 500 nm, which would be applicable to the excitation of various useful fluorescent probes, such as organic compound dyes, Alexa 488, the calcium ion indicator Oregon Green-488 BAPTA-1 (OGB), and the fluorescent proteins EGFP and EYFP. To test the applicability of the CSU10 system with a mercury arc lamp to the fluorescent confocal imaging of dyes that are excited by light from 450 nm to 500 nm, we examined the intracellular Ca^{2+} propagation in HeLa cells using OGB, with a sampling rate of 100 Hz. The fluorescence of OGB loaded into HeLa cells was uniformly distributed in the cytoplasm and the nucleus. After the application of 10 μM histamine (~6 sec after the start of the observation), an increase in Ca^{2+} concentration occurred at the cell periphery that rapidly propagated to the center of the cell (Fig. 5A). The time course of the change in F/F_0 ratio measured in the area enclosed by a white rectangle in Fig. 5B shows an oscillation of intracellular Ca^{2+} concentration with a frequency of approximately 0.1 Hz. This result showed that even at a wavelength of around 500 nm, where no prominent emission lines exist, the CSU10 with a mercury arc lamp could be used to visualize spatial and temporal intracellular Ca^{2+} changes with a time resolution of up to 100 Hz, the same resolution obtained with the CSU10 and a laser light source (Genka *et al.*, 1999).

Multi-color imaging with a half reflective mirror

The wider range of excitation wavelengths emitted by the mercury arc lamp (from 400 nm to 600 nm) allows the visualization of multiple fluorescent dyes. For multi-color imaging with the CSU10, a special interference mirror with multiple transference/reflection peaks (multi-chroic mirror) has been used (Fig. 6A). Since the multi-chroic mirror is

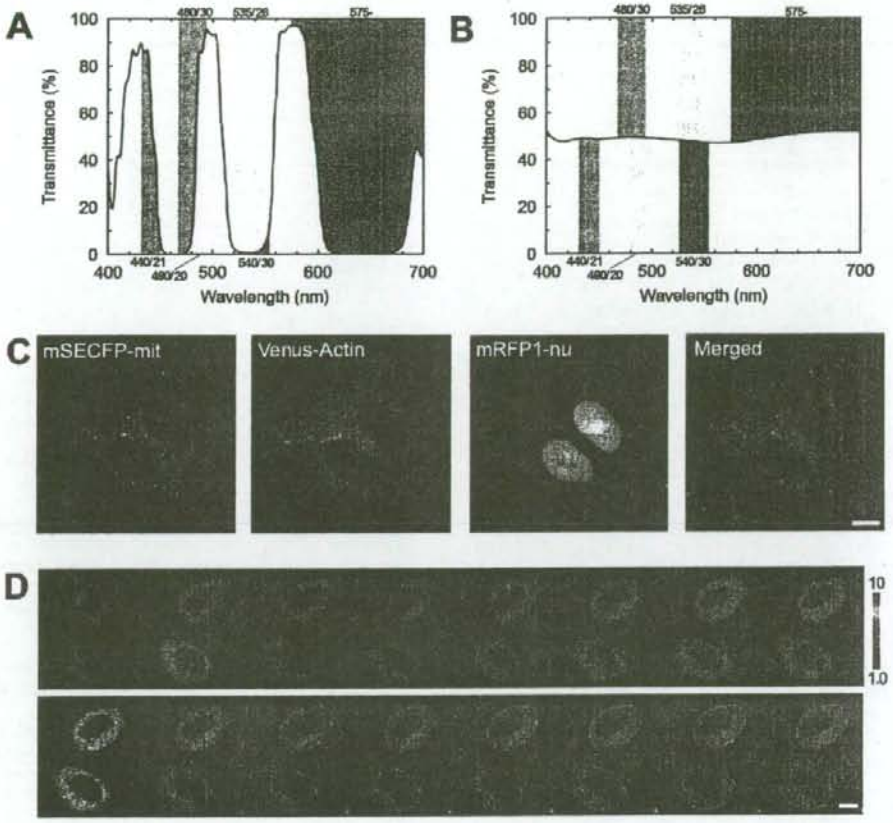

Fig. 6. Multi-color imaging by the CSU10 with a half-reflective mirror. (A) Transmittance of a multi-chroic mirror optimized for three fluorescent proteins: ECFP, EYFP, and mRFP1. (B) Transmittance of the half-reflective mirror, which has about 50% transmittance in the 400–700 nm wavelength range. Areas filled with blue, yellow, or red indicate the amount of light transmitted/reflected by the mirrors and excitation filters and emission filters for ECFP, EYFP, and mRFP1. (C) Images of HeLa cells co-expressing mSECFP-mit, Venus-Actin, and mRFP1-nu. The merged image shows all three channels: green (mSECFP-mit), red (Venus-Actin), and blue (mRFP1-nu). (D) A series of pseudo-colored images of HeLa cells co-expressing YC3.60 (upper panel) and a series of fluorescent images of PKC-γ-DsRed T3 (lower panel). Scale bars in C and D represent 10 μm.

optimized only for cyan, yellow, and red fluorescent dyes, it could limit the advantage of the mercury arc lamp system in providing a broad range of wavelengths. Therefore, to achieve multi-color imaging with the CSU10 with a mercury arc lamp, we introduced a half-reflective mirror instead of the multi-chroic mirror. The transmittance spectrum of the half-reflective mirror is shown in Fig. 6B. Transmission was kept constant at approximately 50% in the 400–700 nm range of the spectrum. By using multiple combinations of excitation and emission filters, multiple images of different colors could be obtained. To compare the transmission/reflection characteristics of the two mirrors described above, the amount of light transmitted/reflected by the mirrors was expressed as areas filled with blue, yellow, and red, if the incident light was an ideal white light (i.e., if the light intensity-wavelength profile were flat). Approximately 50% of the transmitted light through the excitation filter was available for the excitation, and approximately 50% of the collected light through the objective lens could be used for signal detection. The amounts of excitation and emission light in the system using the half reflective mirror were slightly lower than obtained using the multi-chroic mirror. However, the half-reflective mirror should be a powerful choice if one needs to use various combinations of fluorescent dyes for multi-color imaging. To demonstrate the validity of using the half-reflective mirror, we transfected